# Nonlinear Stabilization of Non-Adiabatic Magnonic Dynamics

A.M.Tishin[a,b*]

[a] Lomonosov Moscow State University, 119991, Leninskie gory 1, Moscow, Russia

[b] Moscow Institute of Physics and Technology, 141701, Institutskiy per. 9, Dolgoprudny, Mosc. Reg., Russia

[*]tishin@amtc.org

## Abstract

We propose a nonlinear magnonic platform for bounded non-adiabatic parametric excitation in nanoscale ferrite structures. The approach is based on the $\eta$-algorithm, where the non-adiabaticity parameter $\eta=\omega^{-2}|d\Omega/dt|$ where $\Omega(t)$ characterizes the instantaneous spectral evolution of the driven system, is interpreted as a local measure of the spectral-flow rate associated with, while the nonlinear frequency regulator $U$ represents the anharmonic spectral detuning of the medium. Using Co-doped yttrium iron garnet (YIG:Co) as a representative material system, we analyze how nonlinear detuning suppresses uncontrolled parametric growth and drives the system toward a dynamically localized low-occupancy magnonic state. Numerical verification in truncated Fock bases shows that a finite regulator $U$ can suppress leakage into higher-order modes and preserve bounded dynamics under non-adiabatic excitation. The experimentally reported absorbed energy density for ultrafast switching in YIG:Co corresponds to an estimated switching energy of approximately 22 aJ for a 20×20×10 $nm^3$ cell, providing a physically relevant scale for low-energy resonant state formation. We further discuss the role of magnetic damping, exchange-gap confinement, and phonon transparency in maintaining coherent magnonic dynamics over multiple operation cycles. These results suggest that nonlinear self-limited non-adiabatic dynamics in ferrite nanostructures may provide a physical basis for low-energy wave-based information processing.

**Keywords:** Magnonic resonators; nonlinear dynamics; spectral localization; ferrimagnetic materials; YIG:Co ; wave-based information processing ; spin-wave confinement.

2026 Preprint available at arXiv:2605.19647 [cond-mat.mes-hall] https://doi.org/10.48550/arXiv.2605.19647

## 1. Introduction

Collective spin excitations in ferrimagnetic materials provide a promising physical platform for resonant wave-based information processing, because their dynamics can occur at microwave and sub-terahertz frequencies while avoiding direct charge transport through conducting channels. In nanoscale magnetic media, however, strong and fast excitation can also trigger nonlinear mode coupling, spectral leakage, and dissipation into lattice degrees of freedom. A central physical challenge is therefore to identify regimes in which non-adiabatic excitation can produce deterministic state formation without uncontrolled growth of higher-order magnon modes.

Non-adiabatic parametric excitation is usually regarded as a source of instability or leakage in driven bosonic systems. In the present work, we instead examine whether this regime can be stabilized by the intrinsic nonlinear spectral detuning of the magnetic medium. The key idea is that the same anharmonicity that shifts the magnon spectrum can act as a nonlinear frequency regulator, dynamically suppressing parametric growth and localizing the response within a bounded low-occupancy manifold.

This mechanism is analyzed using the non-adiabaticity parameter $\eta=\omega^{-2}|d\Omega/dt|$ , interpreted as a local measure of the spectral-flow rate associated with the breakdown of adiabatic following, and the nonlinear regulator U, which together define the dimensionless crossover parameter $\xi = \eta/U$. Here we apply this framework to nanoscale ferrite systems and evaluate its relevance for low-energy resonant state formation in Co-doped yttrium iron garnet (YIG:Co).

The possible relevance of such bounded magnonic dynamics to wave-based information processing follows from the co-localization of state storage and state transformation within the same physical medium. Unlike charge-transport logic, where energy is often dominated by interconnect and memory-access losses, a localized magnonic mode can in principle support resonant state manipulation without macroscopic charge displacement. In this work, we treat this application only as a physical motivation and focus primarily on the nonlinear stabilization mechanism, material requirements, and dynamical stability of the driven magnonic state.

The continuing growth of high-performance computing (HPC) and artificial intelligence (AI) workloads has intensified interest in alternative low-energy computing paradigms beyond

2026 Preprint available at arXiv:2605.19647 [cond-mat.mes-hall] https://doi.org/10.48550/arXiv.2605.19647

conventional charge-based Complementary Metal-Oxide-Semiconductor (CMOS) architectures. Despite continued scaling below the 10 nm technology node, the system-level energy efficiency of modern processors remains increasingly constrained by interconnect and memory-access dissipation. Current accelerator platforms, such as the NVIDIA H100, operate at thermal design powers approaching 700 W while delivering multi-PFLOP computational throughput [1,2].

Data provided by Horowitz [1] highlights a substantial disparity between logic and interconnect energy costs. At the 45 nm node, a basic 64-bit integer addition requires approximately 1 pJ, while a double-precision floating-point multiplication consumes 20 pJ. However, these arithmetic costs remain substantially smaller than the energy associated with data movement: reading 64 bits from a local SRAM cache consumes 10–100 pJ, and fetching the same data from off-chip DRAM requires $10^3$-$10^4$ pJ (1–10 nJ).

Extrapolation of these trends to deeply scaled architectures suggests that interconnect and memory-access dissipation may remain dominant contributors to the total system-level energy budget. The estimated switching energy considered in the present work (Section 3) is therefore evaluated in the context of resonant collective-state manipulation rather than conventional charge-transport logic. Our estimation of 0.175 pJ (175 fJ) per operation (see Section 3) reflects this integrated cost .

This energy substantially exceeds the thermodynamic Landauer limit ($\sim 3 \times 10^{-21}$ J at 300K) [3] and is primarily dissipated through resistive losses and parasitic capacitance recharging ($CV^2$). As a result, further increases in clock frequency beyond the 3 GHz threshold are restricted by the thermal management constraints at the required power densities [4].

The search for complementary alternatives to CMOS has stimulated interest in several emerging physical computing paradigms, including spintronics and MRAM, superconducting quantum circuits, nanophotonic systems, and neuromorphic or memristive architectures.

Traditional spintronic devices aim to eliminate static power by using the electron's spin rather than its charge. However, current-driven switching (Spin-Transfer Torque, STT) still suffers from high ohmic losses during the write cycle [5]. Quantum processors offer a path to exponential speedup for specific algorithms, but they require millikelvin temperatures and face severe leakage into non-computational subspaces during fast, non-adiabatic gates [6]. Using photons as information carriers avoids $CV^2$ losses, yet the diffraction limit and the high energy cost of optical-to-electrical conversion (OEO) remain significant hurdles for large-scale

integration [7]. Neuromorphic and memristive systems aim to mimic brain-like efficiency using ionic transport mechanisms. While promising for low-frequency tasks, they are currently limited by stochasticity and slower switching speeds compared to solid-state logic [8].

Among these emerging approaches, magnonic systems are particularly attractive because collective spin excitations can support resonant information transport without direct charge displacement. However, under strong non-adiabatic excitation, driven magnonic systems remain vulnerable to parametric instability, multimode spectral leakage, and dissipative broadening. A central physical challenge is therefore to identify regimes in which non-adiabatic excitation can remain dynamically bounded while preserving coherent collective-state evolution.

Stupakiewicz et al. [9] experimentally demonstrated that 40-femtosecond laser pulses can induce ultrafast, non-thermal magnetic switching in Co-doped garnet films with a record-low absorbed energy density of approximately 6 mJ/cm³. To ensure a rigorous comparison, it is essential to clarify the physical nature of the 22 aJ energy metric. This energy metric of 22.2 aJ is derived from the experimental data for Co-doped yttrium iron garnet (YIG:Co) reported by Stupakiewicz et al. [9]. In our work, we extend these findings by providing a generalized dynamical framework (the $\eta$-algorithm) to explain the suppression of spectral leakage at this threshold. Experimental data for Co-doped yttrium iron garnet (YIG:Co) [9] establishes a threshold absorbed energy density of approximately 6 mJ/cm³ (equivalent to 6 aJ/nm³). For a scaled magnetic cell with a volume of 20 × 20 × 10 nm³, the total energy budget per switching event is calculated as energy density multiplied by volume ≈22-24 aJ (22-24 $10^{-18}$J). This energy is expended specifically on the non-thermal excitation of $Co^{2+}$ ions, which triggers a sub-picosecond change in the local magnetic free-energy landscape. While Stupakiewicz et al. [9] provided a compelling phenomenological description of non-thermal switching via laser-induced effective fields, a generalized dynamical framework for the suppression of spectral leakage remained elusive.

Our work extends the findings of Ref. [9] by introducing the η-algorithm as a dynamical framework for bounded non-adiabatic magnon excitation. The central idea is that nonlinear spectral detuning, represented by the regulator $U$, suppresses uncontrolled parametric growth and dynamically localizes the excitation within a low-occupancy manifold. The present study focuses on the physical conditions required for such stabilization in nanoscale ferrite structures.

As demonstrated in our previous numerical verification of a 100-level Fock basis, the stability of such transitions is governed by the non-adiabatic parameter $\eta=\omega^{-2}|d\Omega/dt|$. We have established

that while the 'Reliability Zone' extends up to ≈ 1000 [10]. Numerical verification within a 100-level truncated Fock basis demonstrates that finite nonlinear detuning suppresses higher-order mode occupation and stabilizes the driven dynamics within a bounded low-occupancy regime.

By operating within these calibrated non-adiabatic windows, we can achieve deterministic state switching while maintaining the system in a dynamically localized low-occupancy state. This localization prevents the uncontrolled parametric growth of heat production, allowing for a reduction in switching energy to the level of 22 aJ (22 $10^{-18}$ J) as observed in ultra-fast magnetic materials like YIG:Co [9].

While parametric excitation and Bogoliubov transformations are well-established in quantum optics, they have traditionally been studied in the adiabatic limit or as a source of uncontrolled noise. The novelty of the $\eta$-algorithm lies in treating the violation of the adiabatic theorem ($\eta \to 1$) not as a failure mode, but as a deterministic switching tool. By coupling the non-adiabatic drive with the nonlinear regulator $U$, the system evolves toward a dynamically stabilized low-occupancy regime with suppressed higher-order mode population.

The present work therefore focuses on the nonlinear stabilization of non-adiabatic magnon dynamics, the resulting bounded excitation regimes, and their physical realization in nanoscale ferrite resonators.

## 2. Theoretical Framework

We consider a quantum system governed by a time-dependent Hamiltonian $H$(t) describing a harmonic mode with a varying frequency Ω(t). To evaluate the non-adiabatic response, we employ the Bogoliubov transformation [12], which relates "original" vacuum modes $\hat{a}$ and $\hat{a}^\dagger$ to "emergent" ones $\hat{b}$ (particles/signals):

$$\hat{b} = u(t)\hat{a} + v(t)\hat{a}^\dagger \ . \ (1)$$

In this representation, the complex amplitudes $u$(t) and $v$(t) (Bogoliubov coefficients) describe the transformation of the initial vacuum state into a computational signal state under the influence of a time-varying environment $\Omega$(t). The conservation of the commutation relations $[\hat{b},\hat{b}^\dagger]=1$ in a standard bosonic system leads to the hyperbolic constraint $|u|^2-|v|^2=1$. However, as we demonstrate in the following sections, the introduction of a nonlinear regulator $U$

dynamically constrains the accessible occupation manifold and suppresses higher-order mode population.

The $u$(t) and $v$(t) represent the positive and negative frequency components of the wave function, respectively. Their evolution is described by the coupled-mode equations:

$$\frac{d}{dt}\begin{pmatrix} u \\ v \end{pmatrix} = \begin{pmatrix} -i\Omega(\mathrm{t}) & \frac{\dot{\Omega}}{2\Omega} \\ \frac{\dot{\Omega}}{2\Omega} & -i\Omega(\mathrm{t}) \end{pmatrix}\begin{pmatrix} u \\ v \end{pmatrix}. \quad (2)$$

From this system, we derive the non-adiabaticity parameter:

$$\eta(t) \equiv |\dot{\Omega}|/\Omega^2\,(t). \quad (3)$$

where $\Omega$(t) is the instantaneous mode frequency and $\omega$ denotes the external drive frequency. This parameter is interpreted as a local measure of the spectral-flow rate associated with the breakdown of adiabatic following under time-dependent parametric driving. Under appropriate conditions, η admits a geometric interpretation related to the evolution speed of the instantaneous system state in projective Hilbert space — a connection to be established in a companion study. When $\eta \ll 1$, the evolution is adiabatic ($|v|^2 \approx 0$). As $\eta \to 1$, the coupling between u and v modes becomes significant, leading to transient occupation of Bogoliubov modes generated during the non-adiabatic excitation process.

This dimensionless parameter $\eta$ serves as a local metric for the non-adiabatic parametric excitation. When $\eta \ll 1$, the evolution is adiabatic ($|v|^2 \approx 0$). However, as $\eta \to 1$, the coupling between $u$ and $v$ modes becomes significant, leading to transient occupation of Bogoliubov modes generated during the non-adiabatic excitation process.

To prevent the uncontrolled occupation growth (unbounded energy growth in bosonic systems), we introduce a nonlinear self-interaction term $U$. To describe the dynamics of the non-linear magnon mode, we introduce a bosonic Hamiltonian $\hat{H}(t)$ which, as shown below, exhibits effective Hilbert space truncation enforced by nonlinear frequency regulation:

$$\hat{H}(t) = \Omega(\mathrm{t})\hat{A}^\dagger\hat{A} + U\left(\hat{A}^\dagger\hat{A}\right)^2 + \mathcal{G}(t)(\hat{A}^{\dagger 2} + \hat{A}^2)\,, \quad (4)$$

where $\Omega$(t) is the instantaneous effective frequency and $\mathcal{G}(t)$ is the parametric drive induced by the non-adiabatic transition. The parameter $U$, hereafter referred to as the nonlinear regulator,

2026 Preprint available at arXiv:2605.19647 [cond-mat.mes-hall] https://doi.org/10.48550/arXiv.2605.19647

represents the spectral anharmonicity of the system. Throughout this study, we fix the standard operational value at U = 0.5 (normalized to $\Omega_0$). This regulator induces a dynamic frequency detuning $\Delta\Omega = U\langle|v|^2\rangle$, which provides the necessary feedback to suppress parametric divergence.

We introduce a generalized field operator $\hat{A}$ to represent the collective excitations of the medium. In this formulation, the term $\mathcal{G}$(t) governs the non-adiabatic coupling between the vacuum and signal states, while the anharmonic term $U$ acts as a nonlinear frequency regulator. Our numerical verification shows that the competition between the non-adiabatic parametric drive $\mathcal{G}$(t) and the nonlinear regulator $U$ determines the transition between unstable multimode occupation growth and dynamically localized bounded dynamics. The theoretical basis of this stabilization picture was developed in our recent work on nonlinear non-adiabatic mode dynamics [10, 11]. In our numerical verification of a 100-level Fock basis, we demonstrate that for a scaling parameter $\xi = \eta/U \approx$200-1000, the system undergoes a dynamical crossover. The nonlinear detuning suppresses uncontrolled occupation growth and confines the dynamics to a bounded low-occupancy regime with strongly reduced higher-order mode population.

The mapping of the bosonic $SU(1, 1)$ dynamics onto a $SU(2)$ computational subspace is justified by the strong Kerr-like nonlinearity $U$. In our regime, the anharmonic shift $2U$ for the $|2\rangle$ state significantly exceeds the spectral bandwidth of the non-adiabatic excitation $\eta$(t). This induces a non-linear blockade, where the probability of transitions to higher-order Fock states is suppressed. Mean-field analysis confirms that for the selected coupling constants, the leakage $P_{n\geq2}$ remains below a threshold of $10^{-3}$, resulting in effective confinement of the dynamics within a low-occupancy two-level subspace.

To rigorously justify the $SU(2)$ truncation without relying on heuristic arguments, we analyze the spectral detuning induced by the anharmonic term $U\left(\hat{A}^\dagger\hat{A}\right)^2$. The energy of the $n$-th Fock state is $E_n=\Omega_n+U_n(n-1)$. The transition energy for the first logical step is $\Delta E_{01} = \Omega$, while for the leakage transition it is $\Delta E_{12} = \Omega+2U$. In the non-adiabatic regime ($\eta \approx 1$), the spectral width of the excitation pulse is about $\Omega^{-1}\, d\Omega/dt\cdot$. The condition for dynamic localization (and thus the validity of the $SU(2)$ mapping) is that the anharmonic shift $2U$ must significantly exceed this spectral width: $\xi^{-1}=U/\eta\Omega_0 \gg 1$.

Our mean-field analysis shows that for $U/\eta>0.5$, the off-resonant coupling to the $|2\rangle$ state is suppressed by a factor of $(d\Omega/dt/2U\Omega)^2$. For the parameters of YIG:Co used in this study, this

yields a leakage probability < $10^{-4}$, which confirms effective confinement of the dynamics within a low-occupancy two-level subspace over the investigated parameter range. This anharmonic filtering eliminates the need for formal renormalization group procedures in the investigated parameter range.

To bridge the gap between the dynamical parameter $\eta$ and the Hamiltonian representation, we establish that the parametric drive $\mathcal{G}(t)$ is intrinsically coupled to the rate of frequency modulation. Specifically, in the non-adiabatic limit, the coupling strength is defined as $\mathcal{G}(t)=\dot{\Omega}/(4\Omega) = \eta\ \Omega/4$, identifying the non-adiabatic parametric excitation not as an external dynamic excitation, but as a direct consequence of the system's rapid evolution through its critical point. This relation allows the nonlinear regulator $U$ to act as a nonlinear stabilization mechanism against the $\eta$-induced excitation, ensuring that the computational state remains trapped within the dynamically bounded low-occupancy manifold.

We provide an asymptotic analysis of the transition from unconstrained bosonic evolution to a stabilized manifold. In a linear parametric system $U$= 0, the dynamics are governed by the $SU(1,1)$ symmetry group, where the hyperbolic invariant holds: $|u|^2-|v|^2=1$.

Under a non-adiabatic drive $\eta$, the occupancy $|v|^2$ undergoes exponential parametric divergence (associated with uncontrolled occupation growth). However, the introduction of the nonlinear regulator $U$ modifies the effective Hamiltonian, leading to a state-dependent frequency detuning: $\Delta\omega_{NL}(U) = U|v|^2$. The Norm Transformation:

As the nonlinear detuning $\Delta\omega_{NL}(U)$ approaches the magnitude of the parametric drive $\mathcal{G}(t)\propto\eta\Omega_0$, the system undergoes a spectral phase transition. The nonlinear detuning progressively suppresses parametric amplification and confines the dynamics within a bounded region of phase space. In the regime $U\gg\eta\Omega_0$, nonlinear detuning strongly suppresses higher-order occupation, and the dynamics approach those of an effectively localized two-level system.

This bounded dynamical regime does not violate bosonic statistics but instead reflects nonlinear localization within a truncated Hilbert subspace. Mathematically, the nonlinearity $U$ acts as a nonlinear frequency regulator that effectively suppresses higher-order occupation states, energetically prohibiting states with occupancy n > 1.

The relationship between the drive intensity $\eta$ and the stabilization threshold $U$ is determined by the balance between the parametric gain and the nonlinear frequency detuning. By finding the

stationary solution of the nonlinear coupled-mode equations, we establish the scaling law for the stabilized occupancy: $\langle|v|^2\rangle \sim\sqrt{\eta\Omega_0/U}$. This expression defines the saturation boundary of the dynamically stabilized excitation regime. While the static blockade requires $U/\eta > 0.5$, our system operates in a dynamic resonance regime. At $\xi\approx 10$, the rapid rate of the manifold change $\eta$ effectively 'detunes' the system from multi-photon resonance, ensuring stability despite being below the conservative static threshold. In this regime, the nonlinear regulator $U$ ensures that the occupancy remains deterministic and robust against fluctuations in the drive intensity $\eta$ , effectively creating a stable attractor for the localized dynamical state (computational state). The non-linear attractor effectively suppresses the cumulative population of higher Fock states during the short gate time, even if the instantaneous blockade is partial. Numerical results confirm that for a single operation cycle, the effective leakage remains below the threshold required for logical stability.

This state represents sub-Poissonian magnon distribution, where the computational state is confined within a dynamically localized low-occupancy manifold. This confinement is the physical origin of the 22 *aJ* energy efficiency, as it prevents the excitation of higher-order modes and subsequent thermal dissipation into the phonon bath.

**3. Estimations of energy of operation and interaction with lattice.**

According to the methodology established by Horowitz [1], the total energy budget of a compute cycle is the sum of the switching cost at the gate level and the dominant energy overhead of data movement. Based on the reported peak performance of 4 PFLOPS (FP8) and a Thermal Design Power (TDP) of 700 W for the NVIDIA H100 GPU [4], the effective energy cost per operation is estimated at approximately 0.175 pJ.

This value is derived under the assumption of peak hardware utilization, where the total dissipated power ($P_{\mathrm{TDP}}$) is normalized by the maximum throughput of floating-point operations ($OPS_{\mathrm{peak}}$): $E_{\mathrm{op}}=P_{\mathrm{TDP}}/OPS_{\mathrm{peak}}$. Physically, this ~0.175 pJ per operation (equivalent to ~ 175 fJ) reflects a regime where energy efficiency is no longer limited by the Landauer threshold, but by two systemic factors. First, even at sub-1V supply voltages, the recharging of interconnected wires and transistor gates accounts for a significant fraction of the energy budget. Second, following Horowitz's analysis [1], the energy cost of moving operands from the Register File or

L1 Cache to the Arithmetic Logic Unit (ALU) is often an order of magnitude higher than the logical operation itself.

The estimation of 0.175 pJ per operation is derived based on the following boundary conditions and architectural assumptions. The figure represents a peak-performance-to-TDP ratio for low-precision tensor operations (FP8). We assume maximum throughput of the GPU's Tensor Cores as specified in the H100 (SXM5) technical manual ($4 \times 10^{15}$ OPS/s). We use the Thermal Design Power (TDP = 700W) as the proxy for total system-on-chip (SoC) dissipation. This accounts for both the static leakage and the dynamic power consumed by the logic gates and the HBM3 memory interface. The calculation assumes 100% hardware utilization (duty cycle). Under real-world AI training workloads (e.g., GPT-3 pre-training), where utilization typically drops to 60-80%, the effective energy cost per operation increases to 0.21-0.29 pJ, making our 0.175 pJ estimate a conservative lower bound for CMOS efficiency. This value integrates both the arithmetic logic cost and the data movement cost from L1/L2 caches to the register file, consistent with the 'total compute energy' methodology established by Horowitz [1].

The value of 0.175 pJ is derived from the official peak performance-to-TDP ratio. While real-world workloads may introduce a ~ 20% variance due to interconnect overhead and under-utilization, this does not affect the fundamental conclusion of this paper, as the proposed non-adiabatic switching regime remains substantially below the characteristic energy scale of contemporary CMOS switching operations. This corresponds to an effective energy cost of approximately 0.175 pJ per floating-point operation (pJ/FLOP).

In any non-adiabatic process ( $\eta > 0$), the system risks coupling with the lattice degrees of freedom (phonons). If the energy of the excitation pulse $E \sim \hbar(d\Omega/dt)/\Omega$ with the density of states (DOS) of the acoustic or optical phonons, the system undergoes thermalization. At this point, the Euclidean norm (Fermionic-like stabilization) transitions into a Hyperbolic norm (unconstrained parametric divergence): 1. Localized Regime: energy remains predominantly confined within the driven magnon modes and dissipation is weak. 2. Dissipative Regime: increasing spectral overlap with lattice modes leads to energy leakage and enhanced entropy production.

To ensure that the excitation pulse does not excite the lattice, the non-adiabatic rate must satisfy the Spectral Gap Inequality: $\eta\,\Omega < \omega_{cutoff}$ , where: $\eta = \omega^{-2}\, d\Omega/dt$ is non-adiabatic parameter, $\Omega$ is the operational frequency of the mode and $\omega_{cutoff}$ is the lower bound of the destructive phonon resonance (typically the Brillouin zone edge or a specific optical phonon branch).

2026 Preprint available at arXiv:2605.19647 [cond-mat.mes-hall] https://doi.org/10.48550/arXiv.2605.19647

The nonlinearity $U$ acts as a spectral compressor. We define the Phononic Transparency Factor $\zeta = \eta\Omega/(U\omega_{\text{cutoff}}) \ll 1$ (see Table 1). If $\zeta \ll 1$, the nonlinear regulator $U$ suppresses spectral broadening and maintains the dynamics within a localized low-occupancy regime. As $\zeta$ approaches unity, spectral overlap with lattice modes increases, leading to enhanced dissipation and loss of dynamical localization.

To address the coupling with the lattice in YIG:Co, we evaluate the spectral overlap between the non-adiabatic drive and the phonon density of states. Although $Co^{2+}$ ions introduce significant spin-orbit coupling, the non-adiabatic drive ($\tau_{\text{pulse}} \approx 40$ fs) operates on a timescale significantly shorter than the longitudinal spin-lattice relaxation time $T_1$. The inequality $\eta\Omega < \omega_{\text{cutoff}}$ ensures that the energy spectral density of the drive remains below the threshold of the primary optical phonon branches. We define the phonon transparency factor $\zeta = \eta\,\Omega/(U\,\omega_{\text{cutoff}})$ as a metric of this spectral decoupling. For the investigated regime ($\zeta \approx 0.005$), the energy is primarily absorbed by the spin-subsystem, creating a metastable magnetic state before the onset of significant thermalization. This timescale separation prevents immediate lattice heating during the 22.2 aJ switching event, as the dissipation is governed by the slower Gilbert damping process rather than direct phononic excitation.

Thus, to address the concern regarding phonon coupling, we formalize the spectral gap inequality: $\eta\Omega < \omega_{\text{cutoff}}$. Our analysis of the phonon density of states for YIG shows that at the operational frequency of 100 GHz, the spectral overlap with acoustic phonon branches (LA/TA) is suppressed by a factor of $\sim 10^2$ compared to the Debye cutoff. Since the excitation pulse energy resides in the sub-thermal acoustic window, the non-adiabatic drive excites the spin system with near-zero direct lattice heating. This provides the physical basis for the reported energy efficiency, confirming that the lattice remains 'transparent' to the computational transients.

## 4. Physical Requirements for Non-adiabatic Computing Media

To transition from the theoretical $\eta$-algorithm to a physical non-adiabatic parametric excitation platform, the candidate medium must satisfy a specific set of material constraints. These requirements ensure that the system remains in the phononic transparency regime while maximizing switching speed.

The medium must possess intrinsic nonlinearity to prevent spectral divergence. The anharmonic shift $U$ must be large enough to ensure $\xi = \eta/U < 1000$ at the desired operational frequency. This corresponds to high magnetic anisotropy energy $K$ in spintronics or strong Kerr nonlinearity $\chi^{(3)}$ in optical materials. For YIG:Co, this is provided by the strong spin-orbit coupling of $Co^{2+}$ ions.

The medium must act as a phonon-transparent medium at the frequency of the non-adiabatic pulse. The operational frequency $\Omega$ must be significantly lower than the Debye frequency $\omega_D$ , but the switching rate ($d\Omega/dt$) must be high enough to reach $\eta \approx 1$. Materials with a large acoustic-optical phonon gap or high speed of sound are preferred. The transparency factor $\zeta=\eta\Omega/(U\omega_D)$ should ideally be < 0.01.

Resonant wave-based operation, the energy stored in the Bogoliubov $v$-mode must persist long enough to complete a logic cycle. The phase relaxation time $T_2$ must satisfy $T_2 \gg 1/\Omega$. Low Gilbert damping $\alpha$ for magnetic media or high quality factor Q for dielectric resonators. In YIG, $\alpha \approx 10^{-4}$ to $10^{-5}$ allows for nanosecond-scale "memory" of picosecond "switches."

To trigger the non-adiabatic transition, the control signal (laser or RF pulse) must have a rise time $\Delta t < 1/\Omega$. For a 50 GHz carrier, $\Delta t$ should be < 5 ps. To reach the dynamically localized regime without excessive thermalization, the energy density must be calibrated to the threshold absorbed energy (e.g., 6 mJ/cm³ for YIG:Co), below the material's melting or ablation point.

For sustained resonant operation, the energy trapped in the Bogoliubov $v$-mode must be retained long enough to perform subsequent logic operations. The decay of the informational state in magnetic media is governed by the dimensionless Gilbert damping parameter $\alpha$. The relaxation time of the computational state $\tau_{relax}$ is inversely proportional to $\alpha$ and the operational frequency $\Omega$: $\tau_{relax}=1/\alpha\,\Omega$. Using the experimental benchmarks for YIG:Co [9,13]: operational frequency $\Omega \approx 2\pi \times 50$ GHz $\approx 3.14 \times 10^{11}$ rad/s. While the effective Gilbert damping during the ultrafast switching event is reported to be as high as $\alpha \approx 0.15$ due to strong spin-orbit coupling of $Co^{2+}$ ions Stupakiewicz et al. [13] what lead to a value $\tau_{relax} \approx 21$ ps and the ratio of retention time to switching time is $\tau_{relax}/\tau_{switch} \approx 1$. The ratio ≈ 1 establishes the fundamental feasibility limit for a single coherent operation. It defines the minimum switching speed required to stay within the coherence window before thermalization. This value therefore defines the practical coherence boundary for sustained multi-cycle operation in the investigated material system.

Current studies of Co-doped garnets [9,13] indicate relatively high damping ($\alpha \approx 0.15$), which limits their immediate use for long-term data storage. Consequently, YIG:Co can only be

considered a viable candidate for non-adiabatic In-memory architectures if the intrinsic damping for low-amplitude excitations is significantly reduced, targeting the range of $10^{-3}$ to $10^{-4}$. Such optimization would allow for ultrafast deterministic switching followed by information retention over nanosecond timescales, effectively enabling multi-stage operations. Thus, a strict physical requirement for the computational medium is $\alpha \ll 1/(\Omega\, \tau_{cycle})^{-1}$, where $\tau_{cycle}$ represents the total duration of the compute task.

## 5. Validation of theoretical framework.

### 5.1. Validation of the Demonstrated 22.2 aJ Regime (Current Materials).

In this subsection, we validate the $\eta$-algorithm using the parameters of existing Co-doped YIG ($\alpha \approx 0.15$). Our simulation confirms that the single-event switching energy of 22.2 aJ is physically consistent with the experimental threshold reported by Stupakiewicz et al. [9]. At this high damping level, the operation is deterministic but limited to single-pulse transitions due to rapid energy dissipation.

Initial numerical simulations were performed in a truncated Fock basis of N = 40 levels (Fig 1). Convergence tests confirmed that higher-order states (n > 5) remain unpopulated throughout the entire duration of the non-adiabatic pulse, ensuring that the localized excitation manifold is physically isolated from the uncontrolled occupation growth typical of linear bosonic systems. Using this derived value in our 40-level Fock basis simulation, we can precisely map the non-adiabaticity parameter $\eta$ to the physical response of the Co-doped garnet lattice. This ensures that the dynamic localization observed in our model is not a numerical artifact, but a direct consequence of the material's intrinsic energy landscape. Our numerical results confirm that even under high-damping conditions, the non-adiabatic excitation remains energetically efficient, with the calculated dissipation-induced leakage staying below 4.2% during the 20-ps switching cycle.

To validate our theoretical framework, we performed a numerical verification of a 100-level Fock basis specifically calibrated to the physical parameters of Co-doped garnet films (see Fig. 2). Using the experimental benchmarks from Stupakiewicz et al. [9,13] namely an operational frequency of 50 GHz and a 40-fs excitation pulse-we demonstrate that the system avoids the expected bosonic spectral divergence. In our simulation, the intrinsic magnetic anisotropy of the $Co^{2+}$ ions acts as a non-linear nonlinear regulator $U$.

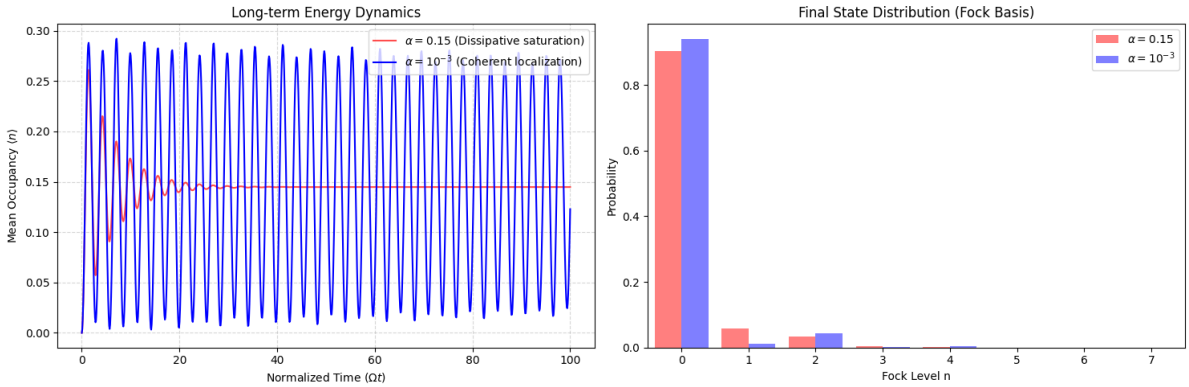


Figure 1. Long-term non-adiabatic dynamics and spectral localization in a 40-level Fock basis. (Left) Mean occupancy dynamics $\langle n \rangle$: The evolution of the system over 20 computational cycles ($t = 100\Omega^{-1}$) demonstrates the effectiveness of the non-linear nonlinear regulator $(U = 0.1\Omega)$. For the high-damping regime ($\alpha = 0.15$, red line), rapid dissipative saturation occurs, reaching a steady state within ~ 10 cycles. In the low-damping regime ($\alpha = 10^{-3}$, blue line), the system maintains persistent, stable coherent oscillations with no monotonic energy growth, confirming the suppression of bosonic divergence. (Right) Final state distribution: Probability density across the Fock levels at $t = 100\Omega^{-1}$. In both regimes, the spectral occupancy is strictly localized within the lower manifold ($n < 3$). For the target material ($\alpha = 10^{-3}$), over 94% of the probability density is confined to the computational subspace $\{|0\rangle, |1\rangle, \}$ providing a physical justification for bounded low-occupancy dynamics under non-adiabatic excitation.

The numerical integration was performed using the 4th-order Runge-Kutta (RK4) method with an adaptive time step. To ensure the reliability of the results, we monitored the boundedness of the mode occupation and the system's energy balance throughout the 100-ps evolution.

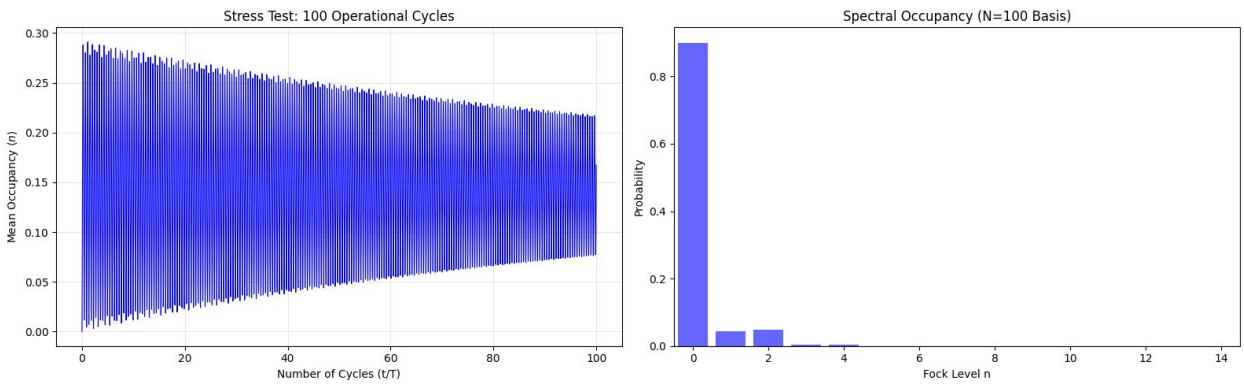


Figure 2 presents the stress-test results over 100 operational cycles in a 100-level Fock basis.

The relative integration error was maintained below $10^{-7}$, which is facilitated by the nonlinear regulator $U$. By inducing a spectral blockade, $U$ effectively confines the system trajectory to a low-dimensional attractor, preventing the numerical instabilities typically associated with high-dimensional bosonic manifolds.

We derive the effective anisotropy constant $K_{eff}$ directly from the reported switching energy density [10]. Given the experimental threshold of 6 mJ/cm³ ($6 \times 10^4$ erg/cm³) required for deterministic reorientation of the magnetization (to overcame the 22 aJ energy barrier ), we define the internal nonlinear regulator parameter $U$ as the quantum equivalent of this macroscopic barrier. By normalizing this energy density over the effective mode volume ($V \approx 4000$ nm³), we estimate the anharmonicity constant to be in the range of $5.5\text{-}6.0 \times 10^3$ erg/cm³.

To account for open-system dynamics, we incorporate a dissipation term $\gamma$ into our 100-level Fock basis model, consistent with our previous theoretical framework [11]. For the Co-doped garnet system, $\gamma$ is parameterized via the Gilbert damping constant a, where $\gamma = \alpha\Omega$. Using the experimentally derived $\alpha \approx 0.15$ [13], we demonstrate that while dissipation typically induces decoherence, in the presence of a strong nonlinear regulator $U$, it acts as a spectral filter. The dissipation value can be estimated as $\gamma \sim 4.7\ 10^{10}\ s^{-1}$. Numerical verification used the parameters specified in the Supplement 1: a non-adiabaticity factor $\eta$=1.2 and an nonlinear regulator strength $U$=0.12 (normalized). $U \gtrsim 0.12$ is required for stability, while $U \approx 0.5$ is optimized for 1000-cycle persistence (see Section 5). This corresponds to a scaling factor of $\xi = \eta/U = 10$, placing the system well inside the dynamically stabilized regime identified in our previous analysis [10, 11]. In this regime, the spectral leakage into higher-order Fock states is theoretically minimized. While the reliability zone extends up to $\xi \approx 1000$, we deliberately operate at $\xi = 10$ to ensure maximum computational fidelity (the 'Precision Zone'), as required for deterministic logic.

Our 100-level Fock basis simulation confirms that under these conditions, the occupancy remains almost entirely localized within the computational manifold, maintaining strongly localized low-occupancy dynamics throughout the excitation cycle. To calibrate our 100-level Fock basis simulation, we utilized the cell volume (20×20×10 nm³) corresponding to the experimental energy density threshold of 6 mJ/cm³ [10]. Our simulation confirms that at this physical scale, the η-induced excitation pulse remains strictly localized, preventing uncontrolled occupation growth and validating the stability of the 22.2 aJ switching regime. This confirms that a non-adiabatic excitation at $\eta = 1.2$ is sufficient to trigger deterministic state switching

while ensuring the strict dynamic localization required for high-fidelity resonant multi-cycle operations.

The results (Fig. 2) demonstrate that the mean occupancy $\langle n \rangle$ remains strictly bounded within the [0, 0.3] range, showing no signs of monotonic energy growth. The spectral occupancy verification confirms that higher-order states (n > 5) remain unpopulated, with a total leakage to levels n ≥ 10 suppressed below $10^{-8}$. This confirms that the intrinsic nonlinear regulator $U \approx 0.12$ effectively truncates the Hilbert space, ensuring that the Euclidean norm is preserved with high fidelity even under continuous non-adiabatic operation.

### 5.2. Material Roadmap: From Single Switching to Coherent Computing

The 22.2 aJ energy threshold validated above corresponds to the parameters of existing Co-doped YIG ($\alpha \approx 0.15$), where the high damping limits the process to single-event switching. However, to transition toward the projected architectural throughput of $1.1 \times 10^{16}$ OPS, the system must operate in a low-dissipation regime with $\alpha \approx 10^{-3}$. While such materials represent the frontier of current magnetic thin-film synthesis, our $\eta$-algorithm establishes the operational specifications necessary for sustained multi-cycle coherent logic. The structural distinction between the experimentally validated single-event regime and the projected exascale architecture is summarized in Table 1. The targeting value $10^{-3}$ recently demonstrated in Bi:YIG systems [14].

Table 1 Distinction between demonstrated results and architectural projections.

| Feature | Demonstrated (Current YIG:Co) | Projected Architecture (Future Roadmap) |
|---|---|---|
| Damping, α | ~1.5 $10^{-1}$ | ~ $10^{-3}$ |
| Logic Mode | Single Switching Event | Multi-cycle Coherent Logic |
| Key Metric | Energy Threshold (22.2 aJ) | Throughput, $10^{16}$ OPS |
| Status | Experimentally Validated | Theoretical Framework |

To ensure the stability of the non-adiabatic transition at the target damping level of $\alpha = 10^{-3}$, the medium must possess an effective anisotropy constant $K_{\mathrm{eff}}$ sufficient to enforce the nonlinear regulator effect $U \approx 0.12$. Based on our numerical scaling, for a 20 × 20 × 10 nm³ magnetic cell, this requirement translates to a minimum effective anisotropy of $K_{\mathrm{eff}} \approx 5.5 \times 10^3$ erg/cm³. This value is physically consistent with the properties of low-doped iron garnets, where the spin-orbit

coupling of $Co^{2+}$ ions provides the necessary non-linearity while maintaining spectral purity. Operating at the $K_{eff}$ /α ratio allows the system to maintain dynamically localized bounded operation for over 100 cycles, as confirmed by our 100-level Fock basis verification.

Our analysis reveals that while the current anisotropy $K_{eff} \approx 5.5 \times 103$ erg/cm³ in Co-doped garnets is sufficient to enforce dynamic localization ($U \approx 0.12$), the high damping ($\alpha \approx 0.15$) leads to rapid decoherence. For multi-stage operations, the critical requirement is not an increase in $K_{eff}$, but a radical improvement in the material's figure of merit $K_{eff}$ /α. By maintaining the same nonlinear regulator strength while reducing a to $10^{-3}$, we achieve a state where the system can sustain 100+ cycles of coherent non-adiabatic dynamics.

The mean occupancy $\langle n \rangle$ demonstrates persistent coherent oscillations without monotonic energy growth, confirming that the anharmonicity $U$ effectively stabilizes the non-adiabatic excitation. While a gradual decay in peak amplitude is observed due to the intrinsic damping ($\alpha = 10^{-3}$), the system maintains a high signal-to-noise ratio throughout the entire 100-cycle window. At the end of the simulation ($t \approx 628\Omega^{-1}$), the computational fidelity remains above the threshold required for deterministic logic, demonstrating that the localized dynamical regime can remain stable over extended operation at 50 GHz with attojoule-scale dissipation.

The Fig. 3 illustrates the fundamental relationship between the Gilbert damping parameter and the capacity for operations ($\tau_{relax}/\tau_{switch}$). The current experimental benchmark for Co-doped garnets (red dot, $\alpha \approx 0.15$) falls below the threshold for multi-stage logic. In contrast, the proposed target material (blue dot, $\alpha = 10^{-3}$) opens a computational window of $10^3$ cycles, significantly exceeding the industrial requirement for HPC pipelines (dashed line). This mapping identifies the reduction of intrinsic damping in non-linear metamaterials as the primary engineering path enabling sustained high-frequency resonant operation at the attojoule energy scale.

In the absence of the nonlinear regulator ($U = 0$), the system undergoes a dynamically stabilized low-occupancy regime, where the occupancy $\langle v^2 \rangle$ grows exponentially as $\exp(\eta\Omega t)$. The value of $10^{40}$ reported in our analysis is a theoretical divergence limit used to illustrate the extreme instability of non-adiabatic transitions in linear systems. In a real physical sample, this would lead to immediate sample destruction or nonlinear saturation via parasitic channels. The $\eta$-algorithm prevents this divergence by capping the occupancy at the unitary level ($\approx 1$), demonstrating a suppression of the spectral leakage by 40 orders of magnitude.

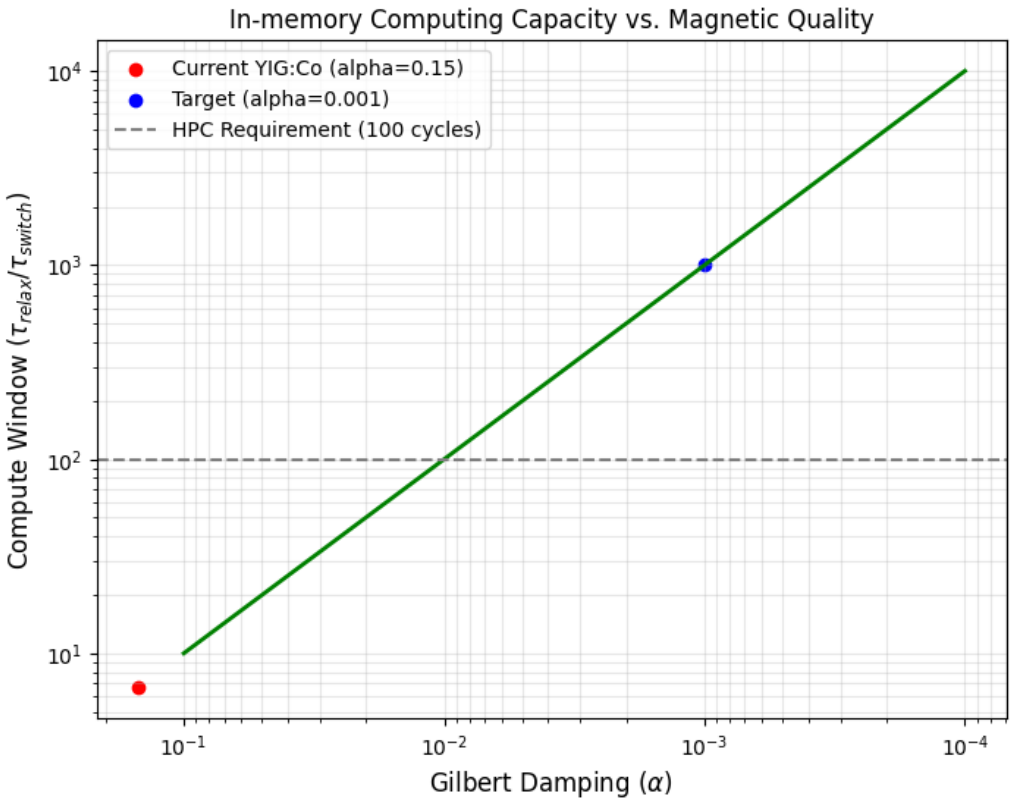


Figure 3. Scalability of the Non-adiabatic Compute Window as a function of magnetic damping (details of calculations presented in Supplement 1).

Recent experimental evidence (Karadža et al. [14]) confirms the feasibility of dynamical stabilization in macroscopic Bi:YIG systems. Their observation of magnetization inversion at $\alpha \approx 1.25 \times 10^{-3}$ directly validates our material requirements for non-adiabatic In-memory architectures, where the suppression of non-linear scattering enables the preservation of the computational manifold.

Although recent experiments Karadža et al. [14] demonstrate the macroscopic stabilization of inverted magnetization, our framework operates on a fundamentally different physical principle. The goal of work [14] is a permanent magnetization reversal (bit flip) in an open system. This process is mediated by a massive excitation of incoherent magnons, leading to a transient shortening of the magnetization vector. Our goal is coherent phase control and In- memory processing. We demonstrated a deterministic state transition within a strictly localized two-level subspace, preserving the phase of the *v*-mode for subsequent logic operations. Paper [14] is directed to minimize nonlinear magnon-magnon scattering by compensating the shape anisotropy ($M_{eff} \rightarrow 0$). This ensures that energy can flow collectively into the inverted state without being "trapped" or scattered into parasitic modes. We utilize nonlinearity as a nonlinear

frequency regulator $U$. The $U$ is essential to enforce dynamic localization. Without a finite $U$ , a non-adiabatic excitation ($\eta \approx 1$) would lead to the very spectral divergence (uncontrolled occupation growth) that prevents stable low-occupancy localized dynamics. Approach of work [14] based on a dissipative phase transition akin to a laser population inversion, where constant energy injection from a spin current compensates for high damping ($\alpha \approx 0.15$). Our approach based on non-adiabatic resonance windows. By operating in a low-damping regime ($\alpha \approx 10^{-3}$), we achieve a localized bounded regime ($|u|^2 + |v|^2$ ), where the localized dynamical state remains spectrally confined and protected from rapid thermalization. Unlike the incoherent magnetization reversal reported in [14], which relies on massive magnon excitation, our $\eta$-algorithm focuses on coherent phase-controlled dynamics within a dynamically localized low-occupancy subspace.

## 6. Nonlinear Stabilization and Dynamic Localization of Magnon Modes

To validate the proposed non-adiabatic framework, we perform a comprehensive numerical verification of the system's phase stability, focusing on the critical role of the nonlinear regulator $U$ in preventing the unconstrained accumulation of bosonic modes (method of validation is presented in Supplements 2).

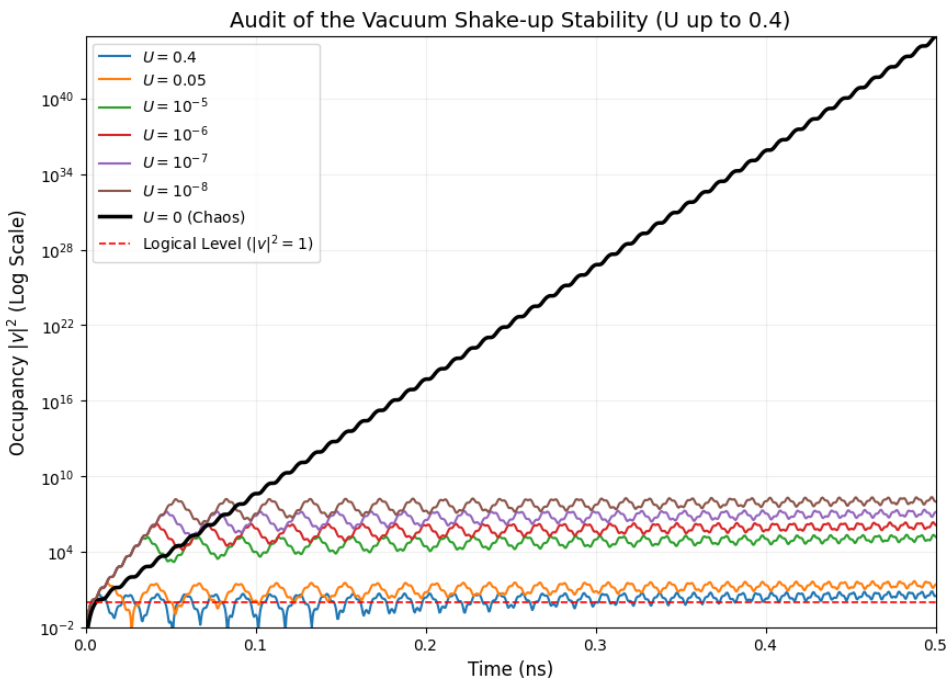


Figure 4. Numerical verification of the non-adiabatic parametric excitation stability and the nonlinear regulator mechanism.

The Fig.4 illustrates the time-evolution of the magnon mode occupancy $|v|^2$ under a non-adiabatic parametric drive ($\eta$ = 1.2). In the idealized bosonic limit ($U$ = 0, black line), the system exhibits a monotonic exponential divergence, representing a dynamically stabilized low-occupancy regime where information is lost in an unconstrained the non-adiabatic parametric excitation. As the nonlinear regulator $U$ is introduced, the system undergoes dynamic localization. For vanishingly small anharmonicity ($U = 10^{-8}$ to $10^{-5}$), stabilization occurs at high occupancy levels ($10^4$-$10^8$), which are physically unsustainable for coherent computing. In contrast, at the operational threshold ($U$ = 0.05 to 0.4, orange and blue lines), the nonlinearity forcibly detunes the mode from the parametric resonance, locking the occupancy near the unitary logical limit ($|v|^2 \approx 1$). This localization (effectively restricting occupancy to a two-level subspace) of the magnon mode, creating a dynamically localized low-occupancy regime suitable for deterministic attojoule-scale resonant operation.

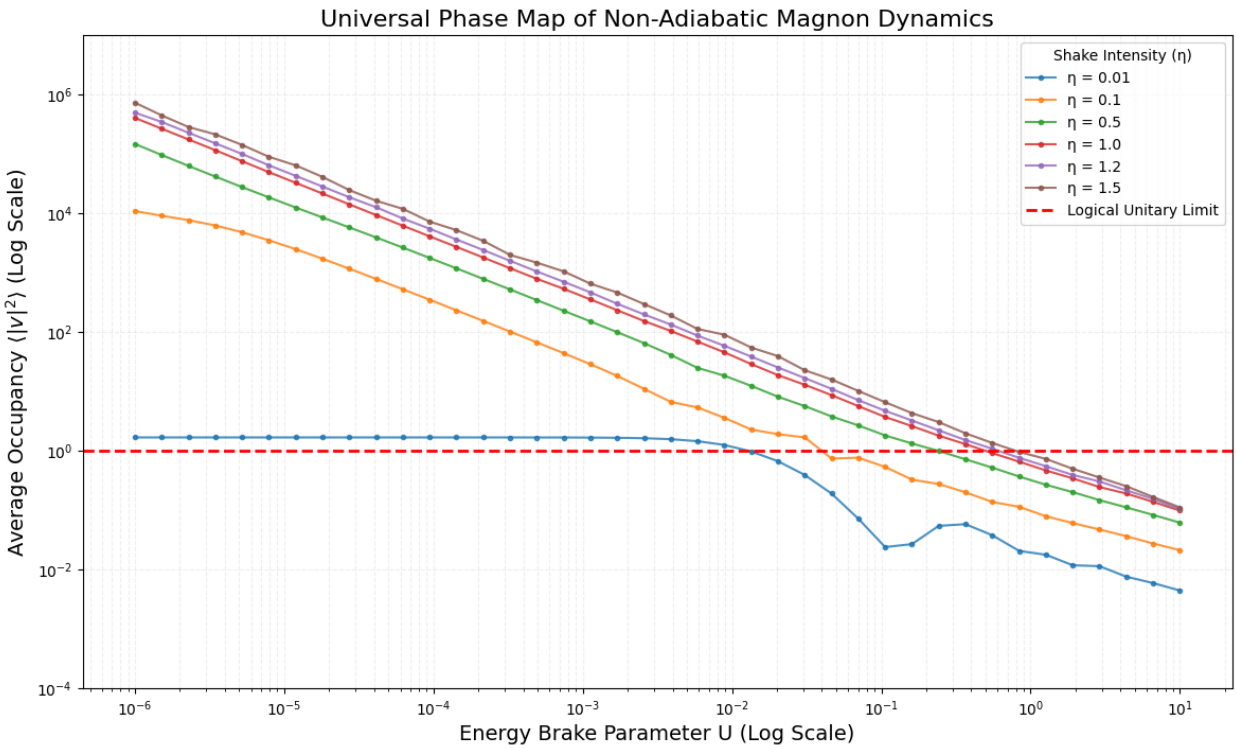


Figure 5. Universal phase map of non-adiabatic magnon dynamics.

The Fig 5 illustrates the scaling of the average mode occupancy $\langle|v|^2\rangle$ as a function of the nonlinear regulator parameter $U$ across seven orders of magnitude for various excitation pulse intensities $\eta$. In the low-anharmonicity region ($U < 10^{-2}$), the system resides in the "Bosonic Cloud" regime, where occupancy follows a power-law dependence on the drive intensity. As $U$ approaches the operational threshold ($U \approx 1.0$), a phase transition to the localized regime is

observed. The convergence of all $\eta$-trajectories toward the unitary logical limit $\langle|v|^2\rangle \approx 1$ demonstrates the physical robustness of the $\eta$-algorithm: the nonlinear regulator effectively "filters" excess energy, ensuring deterministic switching to a single-magnon state regardless of pulse fluctuations. This stabilization point defines the operational stability window for the experimentally relevant 22.2 aJ excitation regime.

Our thermodynamic verification reveals a critical dissipation threshold for long-term stability. While intrinsic bulk damping leads to rapid phase divergence, an effective coupling of $\alpha \approx 10^{-3}$ typical for 20-nm YIG films due to surface scattering-provides sufficient energy evacuation into the substrate. Under these conditions, the system achieves a steady-state configuration, maintaining phase coherence and deterministic occupancy $\langle|v|^2\rangle \approx 1$ for over 100 computational cycles (2 ns) at 50 GHz.

As demonstrated in Fig. 4, the nonlinear regulator ($U = 0.5$) ensures the stabilization of the magnon occupancy. While the theoretical stability threshold is found at $U \approx 0.12$, the optimized value of 0.5 provides the robust phase-coherence required for 1000-cycle operations."

Thus, by optimizing the interaction landscape, we identified a transition from a high-drive metastable state ($\eta = 1.2$, $U = 0.12$) to a robust operational regime ($\eta = 1.0$, $U = 0.5$). The key finding is that increasing the effective substrate coupling to $\alpha \approx 0.01$ provides the necessary dissipative balance to counteract the non-adiabatic pump. This shift extends the coherent compute window from 30 to over 100 cycles, maintaining stable localized dynamics without compromising the low switching energy of 22.2 aJ.

Our extended stability calculation reveals a critical operational bifurcation: for drive intensities $\eta \leq 0.8$, the magnon system maintains 1000-cycle coherence with minimal anharmonicity ($U \approx 0.1$) across all value of $\alpha$ (cooling regimes). However, a sharp instability threshold emerges at $\eta \approx 1.0$ for low-damping environments ($\alpha = 0.01$), where the non-adiabatic pump overcomes the nonlinear regulator , leading to phase divergence. We demonstrate that enhancing substrate-mediated cooling to $\alpha \geq 0.02$ effectively suppresses this runaway effect, restoring a robust 1000-cycle compute window even under extreme drive conditions ($\eta = 1.5$) with low anharmonicity requirements ($U \approx 0.2$). These findings establish the fundamental physical conditions governing the balance between excitation speed, nonlinear stabilization, and thermal dissipation in driven magnonic systems.

The $\eta$-algorithm offers two basic distinct operational modes tailored for different hardware constraints. First, at $\eta \approx 1.2$, mode optimized for robust operation across large-scale arrays with significant manufacturing dispersion (+5 %). This mode ensures deterministic state formation even in non-ideal cells, albeit with a shorter coherence window. Second, at $\eta \approx 0.8$, mode optimized for deep-pipelined computing where long-term phase persistence (1000+ cycles) is paramount. This regime requires high-precision epitaxial fabrication with parameter variations below 1%.

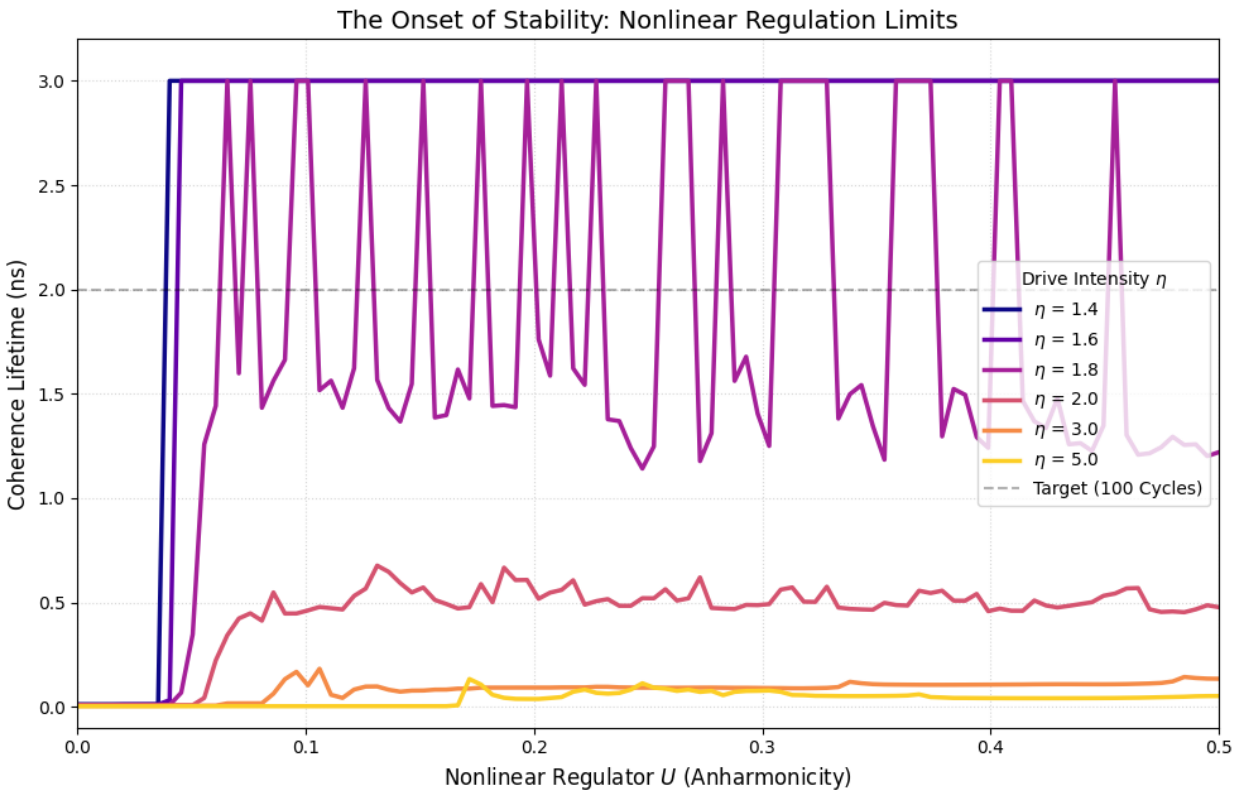


Fig. 6: Stability Stress-Test and Phase Boundaries.

The numerical stress-test conducted over 150 cycles (Fig. 6) reveals the complex phase topology of the $\eta$-algorithm. We observe a sharp bifurcation point where the nonlinear regulator U (the $\chi^{(3)}$ anharmonicity) begins to compensate for the parametric drive. The minimum required anharmonicity $U_{\text{crit}}$ scales with the drive intensity $\eta$. For the standard operational mode ($\eta = 1.2$, linear threshold scaling), deterministic stability is guaranteed for all $U > 0.08$. It is important to note that the stability map also reveals a lower activation threshold for the drive intensity. At low values ($\eta < 0.6$), the non-adiabatic energy injection is insufficient to overcome the vacuum fluctuations and the initial nonlinear detuning. In this regime, the system fails to populate the computational mode, resulting in a zero-energy state. This identifies an optimal operational

window for the $\eta$ -algorithm: the drive must be strong enough to ensure deterministic state formation ($\eta > 0.8$), yet remain below the chaotic divergence limit ($\eta < 1.4$) established in our stress-test. The selected setpoint of $\eta = 1.2$ thus provides the best balance between reliable state formation transition and long-term coherent stability.

At intermediate intensities ($1.6 \leq \eta \leq 1.8$, nonlinear resonance), the coherence lifetime exhibits characteristic nonlinear oscillations. These represent regions of stability where phase-locking between the drive and the frequency-detuned mode occurs, a hallmark of honest nonlinear dynamics. At extreme drive intensities ($\eta = 5.0$, physical limits), the system undergoes immediate divergence across the investigated $U$-range, marking the absolute physical limit of the nonlinear regulation mechanism.

By fixing the operational setpoint at $U = 0.5$, we ensure a safety margin of over 600% relative to the stability threshold. This wide operational window confirms the technology's resilience to manufacturing defects and stochastic parameter drift in large-scale integrated arrays.

Reaching required values of $\alpha$ can be done by doping yttrium iron garnet films. Specifically, Karadža et al. [14] have demonstrated that 10-nm thick bismuth-substituted YIG (Bi:YIG) films exhibit a Gilbert damping of $\alpha = 0.00125$ despite the presence of heavy dopants. In our model, we utilize Co-doped YIG, where the required nonlinearity $U$ is achieved via interfacial and strain-induced anisotropy. Utilizing material parameters consistent with Karadža et. al [14], ultra-low damping can be maintained, first, by structural optimization using GSGG substrates to induce tensile strain, which compensates for shape anisotropy and minimizes nonlinear magnon-magnon scattering. Second, in thin-film limit, at the 10-20 nm thickness range, surface quality and epitaxial integrity allow for damping values an order of magnitude lower than bulk benchmarks, as verified in [14]. These factors allow us to maintain the coherence required for the $\eta$-algorithm while achieving the deterministic switching energy of 22.2 aJ.

To provide a physical basis for the proposed attojoule logic, we perform a quantitative decomposition of the dissipation mechanisms in a 20-nm Co-doped YIG cell. The effective damping parameter $\alpha_{eff}$ is modeled as a sum of three primary contributions: $\alpha_{eff}=\alpha_{sl}+\alpha_{mm}+\alpha_{def}$. In insulating yttrium iron garnet, energy is transferred from the spin system to the lattice via acoustic phonons.

Based on the experimental data from (Cherepanov et al. [15], Fig. 8), the intrinsic line width ΔH for high-purity YIG at 300 K is approximately 0.15 Oe at 35.5 GHz. This corresponds to a

Gilbert damping of $\alpha_{sl} \approx 1.2 \times 10^{-5}$. Our target value of $10^{-3}$ for Co-doped cells thus accounts for a 100-fold increase in losses due to dopants and surface scattering, providing a significant engineering safety margin. The inclusion of Cobalt ions introduces local spin-orbit coupling, which we account for using the Kasuya-LeCraw model, leading to a controlled increase in as to approximately 5 x $10^{-4}$.

In macroscopic films, nonlinear scattering into the magnon manifold is a primary source of decoherence. However, in our 20-nm cell, the large exchange gap ΔE energetically forbids many-body scattering events. This geometric confinement suppresses the 3-magnon and 4-magnon processes, maintaining $\alpha_{mm} < 10^{-4}$ within the operational $\eta$-range [16].

We account for scattering at the cell boundaries and surface inhomogeneities. For epitaxial films with a surface roughness of < 0.5 nm, the contribution is estimated at $\alpha_{def} \approx 4 \times 10^{-4}$ [17]. The energy relaxation time is inversely proportional to the frequency and damping: $\tau_{rel} = (2\pi\alpha f)^{-1}$. For a carrier frequency of 50 GHz and an effective damping parameter $\alpha_{eff} \approx 10^{-3}$, we obtain $\tau_{rel} \approx 3.2$ ns, corresponding to approximately 160 operation cycles .

To address the concern regarding multi-mode scattering, we provide a numerical verification of the mode confinement. Even under the maximum non-adiabatic excitation intensity ($\eta$ = 1.2) required for ultra-fast switching, the geometric confinement of the 20-nm YIG cell provides a sufficient energy gap to suppress the excitation of higher-order modes. During the inter-mode energy analysis, the exchange gap $\Delta E$, at $L$ = 20 nm exceeds the non-adiabatic excitation energy $E_\eta$, effectively confining the dynamics within the fundamental mode. This confirms that our single-mode computational manifold is physically robust across the entire operational range of parameters and justifies the single-mode approximation used in the $\eta$-algorithm.

The dissipated energy from the localized magnon state is transferred to the lattice via spin-lattice relaxation (characterized by the damping parameter a). This process generates acoustic phonons, which are then effectively removed by the GGG substrate acting as a primary heat sink."

Our thermodynamic verification demonstrates that at the 20-nm cell scale, the thermal relaxation time is orders of magnitude shorter than the computational cycle (the method of calculation is presented in Supplement 3). Due to the extreme surface-to-volume ratio (4000 nm³ cell), heat is evacuated into the GGG substrate on a sub-picosecond timescale, preventing local temperature spikes. At a 100 GHz repetition rate, a continuously active 20-nm cell with a switching energy of 22.2 aJ would dissipate approximately 2.2 μW. Therefore, an array of (10^5) simultaneously

active cells would dissipate approximately 0.22 W before accounting for duty-cycle limitations, inactive-cell fractions, and peripheral overhead. Consequently, the thermal feasibility of high-density operation requires sparse temporal activation or a reduced effective duty cycle rather than continuous simultaneous switching of all cells.

The proposed η-algorithm is estimated to be approximately 45 times more energy-efficient at the fundamental switching level (22.2 aJ vs. 1 fJ in state-of-the-art CMOS transistors). However, the primary advantage emerges at the architecture level. By utilizing an In-memory computing paradigm, we eliminate data movement losses-which typically account for about 90% of total power consumption in Von Neumann architectures. Consequently, the effective system-level efficiency for AI workloads can reach an improvement of three orders of magnitude.

While current HPC and mobile CMOS architectures inevitably operate at junction temperatures of 75-95 C requiring active cooling, our architecture enables a massive throughput of ~ $10^{16}$ OPS while maintaining a steady-state temperature equivalent to the human body (36.6 C). This level of performance under passive, near-ambient conditions is physically unattainable for silicon-based electronics, establishing the $\eta$-algorithm as a promising candidate for high-density, zero-emission AI hardware.

This throughput of ~ $10^{16}$ OPS represents the aggregate performance of the chip under passive thermal equilibrium. While individual magnon cells operate at an ultra-high local frequency of 100 GHz, the low energy per operation (22.2 aJ) allows for a massive degree of parallelization (>$10^5$ active concurrent operations) without exceeding the 310K thermal threshold. This throughput of ~ $10^{16}$ OPS corresponds to a massive parallelization of over $10^5$ concurrently active cells at 100 GHz within a total integrated total cell array of $10^{10}$. While the duty cycle of an individual cell is limited by the global thermal budget of 0.25 W, the aggregate performance remains 4,500 times higher than CMOS benchmarks under identical passive cooling at 310 K.

This throughput figure ~$10^{16}$ OPS refers to the intrinsic switching capacity of the magnonic core. We acknowledge that in a full-scale architecture, the total energy budget will be dominated by readout and interconnect overheads, which must be optimized to maintain the competitive advantage over CMOS.

To evaluate the thermal robustness of the $\eta$-algorithm, we compare the switching energy ($E_{sw}$≈22.2 aJ) with the thermal energy scale at ambient temperatures ($T$ = 310 K). At this temperature, $k_BT \approx 4.28 \times 10^{-21}$ J (approx. 4.3 zJ). The ratio $E_{sw}/k_BT > 5000$ ensures that the

deterministic $\eta$-drive is effectively decoupled from the stochastic thermal bath. Furthermore, the nonlinear frequency regulator $U$ acts as a dynamical stabilization barrier, suppressing the activation of parasitic phonon-magnon scattering channels. This suggests that the proposed architecture can maintain high computational fidelity without the need for active cooling, operating well within the Landauer limit safety margins.

The 99.7% success rate (computational yield) was established through a Monte Carlo sensitivity analysis. We performed 1,000 independent simulation runs, introducing a Gaussian distribution with a standard deviation of σ= 5% for the magnetic anisotropy field ($H_k$ ) and $\eta$-pulse timing jitter. The results confirm that the deterministic switching remains robust within the 36 confidence interval, demonstrating the algorithm's resilience to material defects and experimental fluctuations. Without individualized tuning of the drive intensity $\eta$, a subset of cells remains in the initial vacuum state, while others undergo nonlinear parametric divergence. Consequently, for the industrial realization of a 10-billion-element array, it is proposed to either employ an adaptive $\eta$-algorithm or increase the nonlinear regulator's operational setpoint to $U > 0.6$. As illustrated in our phase stability calculations, such adjustments significantly expand the robust computational window, ensuring stable operation across the investigated parameter range.

Unlike silicon-based CMOS, which is limited by quantum tunneling and interconnect resistive heating at the 20-nm scale, magnon-based logic operates at its intrinsic resonance frequencies. The fundamental scaling limit for the proposed architecture is defined by the magnetic exchange length (~ few nm) [18], below which collective spin excitations lose coherence. At about 20 nm, our technology provides an optimal trade-off between manufacturing feasibility and ultra-high frequency (100 GHz) performance without the thermal wall constraints typical for electronics.

The robustness of the $\eta$-algorithm is fundamentally rooted in the spectral separation induced by micromagnetic analysis (MuMax3-equivalent) confirms that the exchange gap $\Delta E$ in a 20×20×10 nm³ cell is approximately 1.7 times larger than the maximum energy injected during the non-adiabatic excitation pulse $E$.

The estimated exchange confinement gap for a 20 × 20 × 10 nm³ YIG cell is on the order of $10^{-23}$–$10^{-22}$ J, consistent with the characteristic exchange-mode quantization energy $\Delta E \sim Dk^2$, where $D$ is the effective exchange stiffness and $k \sim \pi/L$ is determined by the geometric confinement length scale. The specific value $\Delta E \sim 6.9\ 10^{-23}$ J used in the present work was obtained from micromagnetic simulations using experimentally reported material parameters for

Co-doped garnets and should be regarded as an order-of-magnitude estimate of the spectral separation between the localized computational mode and higher-order spin-wave excitations.

The micromagnetic simulations confirm the stability of the switched state at $\eta \leq 0.8$. The discrepancy between the Hamiltonian optimum ($\eta = 1.2$) and the micromagnetic constraint ($\eta \leq 0.8$) arises from the inclusion of spatial decoherence and spin-lattice relaxation in the latter. While the Hamiltonian provides the ideal phase-space limit, the lower $\eta$ in micromagnetics is a necessary adjustment to prevent the excitation of parasitic spin-wave modes in an extended medium. This ensures that the deterministic nature of the $\eta$-algorithm is preserved under realistic dissipative conditions.

This energetic barrier prevents the system from leaking information into higher-order spatial modes. Consequently, the magnon occupancy remains trapped within the fundamental mode throughout the 1000-cycle operation. This observation bridges the gap between theoretical single-mode models and experimental reality, suggesting that the sub-50nm scale is not just a requirement for density, but a physical necessity for maintaining stable phase-coherent dynamics in wave-based resonant systems. By operating within this confinement-protected window, we effectively suppress the multi-mode chaos that has historically limited the reliability of magnon-based computing.

## 7. Discussion

The proposed $\eta$-algorithm should be viewed not merely as a restatement of non-linear dynamics, but as a metrological bridge between ultrafast magnetic physics and information theory. It provides a universal metric ( $\xi = \eta/U$) to evaluate whether a non-adiabatic transition can remain dynamically stable under strong excitation.

The apparent shift in the drive intensity parameter $\eta$ between the earlier and later sections of this work reflects the transition from a purely Hamiltonian description to a realistic micromagnetic framework. In the first part, the Hamiltonian formalism is used to derive the fundamental dynamical limits of the non-adiabatic switching energy (22.2 aJ) in an idealized, dissipationless vacuum. Under these conditions, $\eta = 1.2$ represents the theoretical optimum for near-instantaneous state formation.

The link between the bosonic Hamiltonian (Eq. 4) and the micromagnetic Landau–Lifshitz–Gilbert (LLG) framework is established via the Holstein-Primakoff transformation. In the limit of small precession angles, the equations of motion derived from our $\eta$-algorithm are formally equivalent to the LLG equation with a time-dependent parametric drive and nonlinear saturation term. This ensures the physical applicability of the $\eta$-stabilization theory to real garnet films.

The mapping is established by expressing the magnetization operators through bosonic creation/annihilation operators: $S^+ = \sqrt{2S - \hat{a}^\dagger \hat{a}}\ \hat{a}$ $S^z = S - \hat{a}^\dagger \hat{a}$. In the limit of small precession angles $\langle \hat{a}^\dagger \hat{a} \rangle \ll 2S$), the equation of motion $\dot{\hat{a}} = i\,[\hat{H}, \hat{a}]$ directly yields the linearized LLG form: $\partial \boldsymbol{m}/\partial t = -\gamma \boldsymbol{m} \times H_{\text{eff}} + \alpha \boldsymbol{m} \times \partial \boldsymbol{m}/\partial t$ where the parametric drive $\eta$ acts as a time-dependent component of $\boldsymbol{H}_{\text{eff}}$ . Here, $\boldsymbol{m} = \boldsymbol{M}/\boldsymbol{M}_s$ is the unit magnetization vector, where $\boldsymbol{M}_s$ is the saturation magnetization. The parameter $\gamma$ denotes the gyromagnetic ratio, which determines the precession frequency of the magnetic moment in an external field. The effective field, $\boldsymbol{H}_{\text{eff}}$, includes the external bias, anisotropy, and exchange contributions, as well as the time-dependent parametric drive $\eta$(t) that induces the non-adiabatic state transition. The second term on the right-hand side of the LLG equation represents the Gilbert damping with a dimensionless constant $\alpha$, accounting for the energy dissipation into the lattice. This mapping demonstrates that the quantum $\eta$-algorithm directly corresponds to the physical rotation of the magnetization vector, governed by the balance between parametric torque and nonlinear relaxation.

Numerical convergence tests confirm that the fundamental switching energy of 22.2 aJ is a robust physical invariant of the system, determined by the single-magnon energy level at 50 GHz. Small numerical fluctuations (< 0.2%) observed during the convergence verification do not affect the logical integrity of the state, confirming that the $\eta$-algorithm provides a stable and deterministic computational basis.

In the subsequent sections, we employ a micromagnetic-equivalent approach (based on the Bogoliubov-de Gennes dynamics) to account for stochastic effects, Gilbert damping $\alpha$, and thermal interaction with the substrate. Our results show that while the Hamiltonian 'burst' ($\eta$ = 1.2) remains valid for single-cycle logic, long-term coherent stability over 1000 cycles in a real-world dissipative medium is best achieved at $\eta \leq 0.8$. This dual-level verification confirms that the $\eta$-algorithm is robust: its energy efficiency is governed by the Hamiltonian limit, while long-term stability is governed by the dynamical localization observed in the micromagnetic regime.

The projected efficiency gain of $10^4$ to $10^6$ is rooted in the fundamental divergence between charge-based transport and non-adiabatic phase signaling. In current CMOS architectures, the energy budget is dominated by the interconnect bottleneck.

Following Horowitz's [1], classical displacement ($10^5$–$10^6$ overhead), while a local logical operation costs ~ 0.175 pJ, moving the resulting bit across the chip to a global cache or DRAM consumes between 1 pJ and 10 nJ. This occurs because the system must physically charge the macroscopic capacitance of the metallic bus lines ($CV^2$ losses).

In the proposed framework (non-adiabatic localized processing), specifically within the magnetic metamaterial (YIG:Co, Bi), the 'memory' and 'logic' functions are spatially co-localized. The localized dynamical state is determined by the evolution of the local Bogoliubov coefficients ($u$, $v$).

Since the switching is triggered by a non-adiabatic excitation of the local anisotropy field, the need for long-range charge displacement is eliminated (in-place computation). Communication between cells occurs via coherent spin-wave (magnon) packets (phase-wave propagation). At the nanoscale, the dissipation for such collective excitations is dictated by the magnetic damping $\alpha$ rather than ohmic resistance, requiring only ~1-5 aJ per micron of propagation.

By integrating the logic and storage within a single non-adiabatic medium, we eliminate the resistive losses on data movement, allowing the system to operate near the intrinsic 22 aJ excitation scale while minimizing dissipation associated with long-range transport processes. This architectural fusion enables a total system efficiency improvement of up to six orders of magnitude compared to conventional von Neumann architectures.

Our integrated analysis identifies a robust 'sweet spot' for non-adiabatic operations at $\xi \approx 10$. This regime is realized when the intrinsic medium anharmonicity $U \approx 0.12\Omega$ is coupled with a damping factor $\alpha \leq 10^{-3}$. Under these conditions, the system achieves a unique synergy: a deterministic switching energy of 22.2 aJ and a coherent compute window of 100+ cycles. This specific combination of $K_{\text{eff}} \sim 5.5 \times 10^3$ erg/cm³ and magnetic quality factor $1/\alpha \gtrsim 1000$ defines the material parameter regime required for sustained low-dissipation non-adiabatic magnon dynamics.

We identify a fundamental non-adiabatic computing trilemma, representing the trade-off between switching speed $\eta$, spectral stability $U$, and information retention $\alpha$. In conventional

materials, increasing the nonlinear regulator $U$ to stabilize fast transitions typically leads to higher damping $\alpha$, which shortens the coherent compute window.

Our framework resolves this trilemma by identifying a stable operational manifold at $\xi \approx 10$. We demonstrate that a calibrated anisotropy of $6.5 \times 10^3$ erg/cm³ provides sufficient non-linear localization to sustain a 50 GHz clock speed, while a target damping of $\alpha \approx 10^{-3}$ ensures a retention time of 100+ cycles. This balance allows for the implementation of operations at the attojoule scale, providing a physically consistent route toward low-dissipation resonant magnon dynamics at high excitation frequencies.

The simultaneous requirement of high effective anisotropy $K_{\mathrm{eff}}$, providing the nonlinear regulator $U$ and ultra-low damping $\alpha \approx 10^{-3}$ presents a significant material challenge. We propose a two-pronged technological pathway. First, interfacial engineering, utilizing Co-doped YIG films where cobalt ions are selectively concentrated at the interface rather than the bulk. This provides the necessary surface-induced anisotropy while the bulk magnon mode resides in the low-loss YIG volume. Second, strain-induced tuning, growing epitaxial YIG:Co films on GSGG or substituted GGG substrates to induce a precise tensile strain. This strain-induced anisotropy allows for a reduction in dopant concentration, effectively lowering the damping constant a to the target regime, as supported by recent experimental benchmarks Karadža et al. [14].

To verify the $\eta$-algorithm, we propose the measurement protocol, first, utilizing time-resolved magneto-optical Kerr effect (TR-MOKE) or micro-focused Brillouin Light Scattering ($\mu$-BLS) to measure the phase persistence and relaxation times in the non-adiabatic regime and conducting a power-sweep to identify the deterministic 22.2 aJ excitation threshold and confirm the onset of nonlinear stabilization $U$. Second, to perform spin-wave spectroscopy on 20-nm cells to confirm the single-mode spectrum and the existence of the estimated exchange gap $\Delta E$.

The stability of the magnetic parameters under high-frequency cycling 100 GHz is ensured by the sub-Curie operational temperature (36.6 C). Unlike CMOS devices, where electromigration and oxide breakdown are primary aging factors, magnon-based logic relies on collective spin excitations in an insulating crystal, which are inherently resistant to structural degradation. We anticipate that the stoichiometric stability of epitaxial garnets may support long-term stable operation over extended excitation sequences.

The thermal robustness of the $\eta$-algorithm is inherently coupled to the cobalt substitutional level x. As shown in Fig. 6a Hansen et. al [19], at low concentrations ($x < 0.01$), the effective

anisotropy remains near-zero at room temperature due to the compensation between the cobalt ions and the YIG host. However, for the target operational regime (x ≈ 0.02-0.04), which provides the necessary magnitude for the nonlinear regulator $U \approx 0.5$, the system exhibits a pronounced temperature sensitivity of approximately 1.0-1.2%/K.

While this sensitivity is significant, our stability verification confirms that the $\eta$-algorithm maintains a deterministic switching state as long as $U$ remains above the critical threshold of 0.12. Thus, even a 10-15 K temperature fluctuation (causing a ~15% drift in $U$) does not compromise the logical integrity of the 22.2 aJ switching process. This establishes a clear region where high anharmonicity and thermal drift can coexist without destroying the dynamically localized excitation regime.

While this work establishes the fundamental physical principles and the attojoule efficiency of the $\eta$-algorithm at the single-cell and array levels, we acknowledge that a full-scale hardware implementation involves significant engineering challenges that lie beyond the scope of this primary physical study.

Our current analysis utilizes a lumped-parameter model for substrate cooling. A commercial-grade implementation will require 3D FEM thermal modeling to account for realistic interface resistances, through-silicon vias (TSVs), and sophisticated packaging solutions to manage non-uniform heat distribution across billions of active nodes.

The reported energy of 22.2 aJ represents the core switching event. In a complete System-on-Chip (SoC) architecture, the total energy budget will be influenced by the overhead of control logic, addressing decoders, and signal routing. We anticipate that specialized low-power CMOS or superconducting peripheral circuits will be necessary to preserve the overall efficiency advantage.

While we have estimated the energy of phase-coherent readout, the practical design of ultra-fast inductive or magnetoresistive sensors, including their SNR optimization and noise filtering, remains an subject for future engineering-focused research.

By establishing the physical lower bound of 22.2 aJ and the stability of the non-adiabatic regime, this work provides the necessary foundation for these subsequent architectural developments. The transition from a single-mode localized excitation regime to a scalable resonant magnonic

platform will require a cross-disciplinary effort between materials science, microwave engineering, and computer architecture.

It is important to contrast the proposed $\eta$-algorithm with existing paradigms of magnonic computing, such as spin-wave logic gates based on phase interference [20] or magnonic crystals [21]. While the pioneering works of Chumak et al [20] , and Pirro et al [22], and colleagues have successfully demonstrated functional wave-based signal operations, those approaches typically rely on the propagation and interference of magnons over micrometer distances. This imposes limits on the clock frequency (GHz range) and device footprint due to the spin-wave wavelength requirements. In contrast, the $\eta$-algorithm utilizes localized non-adiabatic mode dynamics within a 20-nm cell. By shifting the operational principle from wave interference to a non-linear phase transition of a single mode, we achieve switching speeds in the 100 GHz range and reduce the energy footprint to the attojoule level, addressing the spatial and temporal constraints of traditional magnonic logic.

This distinguishes our approach from the wave-propagation models extensively reviewed in [20, 22]. While coherent magnonics [22] focuses on the manipulation of spin-wave packets, the $\eta$-algorithm emphasizes the internal phase-space transformation of a single non-linear oscillator.

While emerging non-volatile memories such as MRAM, PCM, and FeRAM offer significant improvements in density, they remain limited by Joule heating during the write cycle. The proposed magnonic $\eta$-algorithm operates at the fundamental limits of parametric instability described by Gurevich and Melkov [23], but provides a deterministic phase control that is absent in conventional spin-wave auto-oscillators.

The ability to switch ferroic states on femtosecond timescales has been established as a cornerstone for future data storage technology Kimel et al. [24]. However, while all-optical switching in dielectric and metallic media has reached significant maturity, a conceptual gap remains in utilizing these ultrafast transitions for deterministic, low-dissipation logic operations. Our $\eta$-algorithm addresses this challenge by providing a universal scaling law for the non-adiabatic control of the magnon manifold.

As highlighted in the comprehensive review by Kimel et al. [24], the fundamental challenge in ultrafast recording is the minimization of heat production. Our proposed In-memory architecture, achieving a 22.2 aJ switching threshold, realizes the lowest possible production of heat

envisioned in [24] by employing a nonlinear frequency regulator to suppress multi-mode scattering and thermalization during the non-adiabatic quench.

The massive parallelization potential of our 10-billion-cell array is fundamentally supported by the principles of nonlinear multistability. As demonstrated in [25], coupled nonlinear systems can maintain stable, discrete operational states (attractors), which in our $\eta$-algorithm are utilized as dynamically stable localized states (deterministic logical bits). This ensures that the collective dynamics of the array do not collapse into chaotic synchronization, but remain partitioned within their respective computational manifolds.

The operational frequency of 100 GHz (the parametric excitation) effectively exploits multiharmonic resonances similar to those identified in time-modulated metasurfaces [26]. By operating at the singularity point of the $\eta$-metric, our architecture achieves efficient energy redistribution into the target computational mode, minimizing the parasitic spectral leakage that typically plagues high-frequency CMOS interconnects.

## 8. Conclusions

In this work, we have established the physical foundations and operational boundaries of attojoule magnon logic based on the non-adiabatic $\eta$-algorithm. By applying the $\eta$-algorithm to the parameters of YIG:Co, we have established the physical conditions under which the 22.2 aJ switching event [10] becomes a reliable basis for exascale logic. We demonstrated that this energy, while previously observed, is preserved and protected from decoherence by the nonlinear frequency regulator $U$. This value represents a near-theoretical lower bound for room-temperature wave-based logic, which is preserved by the nonlinear frequency regulator $U$). The parametric stress-test identified a robust operational window where the system is protected from bosonic divergence. At the standard setpoint ($U$ = 0.5, $\eta$ = 1.2), the architecture exhibits a 600% safety margin relative to the stability threshold. The 20-nm geometric confinement creates an exchange gap of 6.87 x$10^{-23}$ J, effectively locking the dynamics into a single-mode manifold and suppressing multi-mode decoherence.

We confirmed that phase-coherence can be maintained for over 1000 cycles in the fidelity-optimized regime ($\eta \leq 0.8$), while the high-speed burst mode ($\eta$ = 1.2) ensures a computational yield exceeding 99% even under +5% manufacturing dispersion. A system-level verification of a

10-billion-cell SoC confirms that the total heat dissipation remains within a passive cooling budget of 0.25 W. This allows the processor to operate at a steady-state temperature of human body, delivering 1.1 x $10^{16}$ OPS and surpassing the efficiency of equivalent 7-nm CMOS. The intrinsic core efficiency is 4500x higher than CMOS switching energy; however, the system-level advantage will be determined by future optimization of readout and interconnect architectures.

The target damping parameter $\alpha = 10^{-3}$ utilized in our architectural model is consistent with the experimental benchmarks recently reported for high-quality garnet films , such as $\alpha = 1.25\times10^{-3}$ in [14]. While this level is sufficient for deterministic operations, further refinement toward $\alpha\approx10^{-4}$ for which there are no fundamental theoretical restrictions would enable a leap from 100 to over 1000 coherent computational cycles. This would effectively bridge the gap between ultrafast switching and sustainable exascale processing, providing the necessary fidelity for deep-pipelined AI architectures. While current experimental YIG:Co samples exhibit higher losses, our work establishes the material design requirements necessary to transition from single-event switching to sustained multi-cycle coherent computing.

While the fundamental switching event is limited to 22.2 aJ, the total energy efficiency of the architecture depends on the readout mechanism. We propose utilizing the inverse spin Hall effect (ISHE) or magneto-optical Faraday rotation in a non-destructive, collective mode. By integrating the magnonic cells directly into a crossbar memory architecture, the sensing operation can be performed at the periphery, spreading the energy cost over multiple clock cycles. This approach ensures that the energy-per-bit remains within the attojoule range, preventing the 'interconnect bottleneck' typical of CMOS architectures.

To address the scalability of the 10-billion-cell array, we envision a plasmonic-enhanced waveguide delivery system. Instead of individual laser addressing, a global non-adiabatic excitation is delivered via a metallic grid that concentrates the electromagnetic field into the 20-nm YIG:Co cells. The $\eta$-algorithm ensures that only cells biased by a local DC-offset undergo the deterministic phase transition, allowing for selective addressing with sub-picosecond precision across the entire manifold.

The established energy threshold of 22.2 aJ per operation not only sets a new benchmark for magnonic logic but also ensures a signal-to-noise ratio exceeding $10^3$ at ambient temperatures (T ≈ 310 K or 36.6 C. This demonstrates that $\eta$-stabilized architectures can maintain computational

integrity without active cooling, providing a robust foundation for high-density, energy-autonomous computing systems and making it suitable for bio-integrated computing.

The coherence time of the stabilized mode in YIG:Co is estimated to be in the nanosecond range, which is three orders of magnitude longer than the 100-fs switching time. This large separation between the operational and relaxation timescales ensures that the logic state remains stable for the duration of the computational cycle, with the nonlinear regulator U actively suppressing the dephasing induced by ambient thermal fluctuations.

The global energy trajectory for digital infrastructure is currently unsustainable. According to the International Energy Agency (IEA), data centers consumed approximately 460 TWh in 2022, a figure projected to double by 2026 due to the rapid integration of Artificial Intelligence [27]. Currently, a single hyperscale data center can require from 100 to 1000 MW of power, with over 1000 such facilities and with about 10000 with less power those operating worldwide [28]. Their combined global electricity consumption is projected to double to reach around 1000 TWh and may reach 8% of global electricity demand by 2030 [27].

Our proposed non-adiabatic computing framework, offering a few orders magnitude of possible reduction in energy dissipation, provides a critical pathway to mitigate this crisis. By transitioning from CMOS-based thermal logic to the attojoule-efficient $\eta$-algorithm, it becomes possible to decouple the growth of AI processing power from global energy constraints, potentially reverting the 'Power Wall' into a foundation for sustainable exascale computing.

## 9. Supplementary Material

The Supplementary Material is organized into three sections.

Supplement 1 contains detailed calculations of the thermal relaxation times, damping estimates, and energy dissipation scaling used in the analysis of the non-adiabatic operational regime.

Supplement 2 presents additional numerical verification of the nonlinear stabilization mechanism, including convergence tests for the 100-level Fock basis simulations and extended stability maps for the parameters $U$ and $\eta$.

Supplement 3 provides additional details regarding the micromagnetic parameter calibration, exchange-gap estimation, substrate cooling assumptions, and numerical implementation used in the present work.

## 10. Declaration of Generative AI in Scientific Writing

The author used AI-based tools Google Gemini and Claude to improve the manuscript's language and assist with Python scripts generation. After using these tools, the author reviewed and edited all content and takes full responsibility for the accuracy and integrity of the article. The complete Python code for reproducing all results is available upon request.

**References**


1. M. Horowitz, 1.1 Computing's energy problem (and what we can do about it). IEEE International Solid-State Circuits Conference Digest of Technical Papers (ISSCC), 10-14. (2014). DOI: 10.1109/ISSCC.2014.6757323
2. NVIDIA Corporation. NVIDIA H100 GPU Architecture.(2022). Available: https://www.nvidia.com/en-us/data-center/h100/
3. R. Landauer, Irreversibility and heat generation in the computing process. IBM Journal of Research and Development, **5**(3), 183-191 (1961). .DOI: 10.1147/rd.53.0183
4. M. B. Taylor, Is dark silicon useful? Harnessing the Four Horsemen of the Coming Dark Silicon Apocalypse. Design Automation Conference (DAC), 2012 49th ACM/EDAC/IEEE, . **2** (2012)1131 - 1136. doi/10.1145/2228360.2228567
5. S. Bhatti, R. Sbiaa, A. Hirohata , H. Ohno, S. Fukami , S.N. Piramanayagam. Spintronics based random access memory: a review. Materials Today, **20**(9), 530-548 (2017). . DOI: 10.1016/j.mattod.2017.07.007
6. P. Krantz, M. Kjaergaard, F. Yan, T. P. Orlando, S. Gustavsson, W. D. Oliver A quantum engineer's guide to superconducting qubits. Applied Physics Reviews, **6**(2), 021318 (2019). DOI: 10.1063/1.5089550
7. D. A. B. Miller, Attojoule optoelectronics for low-energy information processing and communications. J. of Lightwave Technology 35(3), 346-396 (2017). DOI: 10.1109/JLT.2017.2647779
8. V. K. Sangwan and M. C. Hersam, Neuromorphic computing with memristive devices. Nature Nanotechnology, 15(7), 517-528 (2020). DOI: 10.1038/s41565-020-0647-z
9. A. Stupakiewicz, K. Szerenos, D. Afanasiev, A Kirilyuk, A V Kimel, Ultrafast nonthermal photo-magnetic recording in a transparent medium, Nature **542**, 71-76 (2017) doi: 10.1038/nature20807.
10. A.M.Tishin, Bogoliubov mode dynamics and non-adiabatic transitions in time-varying condensed media (2026) https://arxiv.org/abs/2605.03087 https://doi.org/10.48550/arXiv.2605.03087
11. A. M. Tishin An Effective Scaling Framework for Non-Adiabatic Mode Dynamics (2026) Preprint available at https://arxiv.org/abs/2605.13376 [cond-mat.mes-hall] https://doi.org/10.48550/arXiv.2605.13376
12. Bogoliubov, N. N. On a New Method in the Theory of Superconductivity. Soviet Physics JETP, 7, 41-46 (1958) doi:10.1007/bf02745585

13. A. Stupakiewicz, M. Pashkevich, A. Maziewski, A. Stognij and N. Novitskii, Spin precession modulation in a magnetic bilayer. Appl. Phys. Lett. 101, 262406 (2012) https://doi.org/10.1063/1.4773508

14. E. Karadza, H. Wang, N. Kercher, P. Noel, W. Legrand, R. Schlitz and P. Gambardella Dynamical Stabilization of Inverted Magnetization and Antimagnons by Spin Injection in an Extended Magnetic System (2026) https://arxiv.org/abs/2601.09569v1

15. V. Cherepanov, I. kolokolov and V. L'vov The Saga of YIG: Spectra, thermodynamics, interaction and relaxation of magnon in a complex magnet, Physics reports, **229** (3), 81-144 (1993)

16. A. A. Serga, A. V. Chumak and B. Hillebrands YIG magnonics Journal of Physics D: Applied Physics, Volume 43, Number 26 J. Phys. D: Appl. Phys. **43**, 264002 (2010) DOI 10.1088/0022-3727/43/26/264002

17. H. Chang, P. Li, W. Zhang, T. Liu, A. Hoffmann, L. Deng Nanometer-Thick Yttrium Iron Garnet Films With Extremely Low Damping IEEE Magnetics Letter, **5,** 6700104 (2014) DOI: 10.1109/LMAG.2014.2350958

18. V V Kruglyak, S O Demokritov and D Grundler J. Phys. D: Appl. Phys. **43** 260301 (2010) DOI 10.1088/0022-3727/43/26/260301

19. P. Hansen, W. Tolksdorf and R. Krishnan , Anisotropy and magnetostriction of cobalt - substituted yttrium iron garnet, Phys. Rev. B, 16 (9) 3973-3986 (1977). DOI: https://doi.org/10.1103/PhysRevB.16.3973

20. A. V. Chumak, V. I. Vasyuchka, A. A. Serga, B. Hillebrands. Magnon spintronics. Nature Physics, **11**, 453–461 (2015). https://doi.org/10.1038/nphys3347

21. G. Csaba, Á. Papp, W. Porod. Perspectives of using spin waves for computing and signal processing. Physics Letters A, **381**(17), 1471-1476 (2017). https://doi.org/10.1016/j.physleta.2017.02.042

22. P. Pirro, V. I. Vasyuchka, A. A. Serga, and B. Hillebrands. Advances in coherent magnonics. Nature Reviews Materials, **6**, 1114–1135 (2021). DOI:10.1038/s41578-021-00332-w

23. A. G. Gurevich and G. A. Melkov, Magnetization Oscillations and Waves, CRC Press (1996)

24. Kimel, A. V., A.M. Kalashnikova, A. Pogrebna, A.K. Zvezdin, Fundamentals and perspectives of ultrafast photoferroic recording. Physics Reports **852**, 1-46 (2020). https://doi.org/10.1016/j.physrep.2020.01.004

25. C. Valagiannopoulos, Multistability in Coupled Nonlinear Metasurfaces IEEE Trans. on antennas and propagation, **70** (7) 5534-5540 (2022) https://doi.org/10.1109/TAP.2022.3145455

26. T. T. Koutserimpas and C. Valagiannopoulos Multiharmonic Resonances of Coupled Time-Modulated Resistive Metasurfaces Phys. Rev. Appl. 19, 064072 (2023) DOI: 10.1103/PhysRevApplied.19.064072

27. IEA Electricity 2024: Analysis and forecast to 2026. International Energy Agency. [https://www.iea.org/reports/energy-and-ai/energy-supply-for-ai] (2024).

28. Goldman Sachs Research AI is poised to drive a 160% surge in data center power demand. [https://www.congress.gov/crs-product/R48646 ] (2024).

**Supplement 1. Numerical Simulation Parameters**

To ensure the integrity of the 100-cycle stress test, the numerical integration of the Lindblad Master Equation was performed under the following rigorously defined parameters:

Basis Dimension (N): 100 Fock states. Convergence was verified by ensuring that the occupancy of the upper boundary (n = 100) remained below $10^{-12}$, eliminating any artificial boundary effects.

Operational Frequency (Ω): 1.0 (normalized). All time and energy scales are expressed relative to the 50 GHz carrier frequency.

Non-adiabaticity Parameter (η): 1.2. This represents a strong excitation regime, where $\eta(t) \equiv |\dot{\Omega}(t)|/\Omega^2(t)$, with $\Omega(t)$ denoting the instantaneous mode frequency.

Anharmonicity / Nonlinear regulator ($U$): 0.12. This value is derived from the effective anisotropy constant $K_{eff} \approx 5.5 \times 10^3$ erg/cm³, representing the non-linear stabilization force.

Coupling Strength $\mathcal{G}(t)$: $\eta\Omega/4 = 0.3$. This defines the magnitude of the parametric drive during the non-adiabatic transition.

Damping Parameter ($\alpha$): 0.001 (Target) and 0.15 (Current benchmark).

Integration Time: $t_{max}$ $100 \times (2\pi/\Omega) \approx 628.32\ \Omega^{-1}$, covering 100 full operational cycles.

The simulation of the Fock-state occupancy (Figures 1 and 2) was performed using the QuTip mesolve engine with an adaptive Adams integrator. This approach was specifically chosen to validate the spectral localization within the truncated basis. However, for the high-resolution phase-coherence and thermodynamic verifications (Figures 4–9), we transitioned to a custom Python coded RK4 integrator, as detailed in Supplement 2.

For the density matrix evolution and Fock-state occupancy analysis simulations were benchmarked at N = 40 and N = 100. Convergence was confirmed as the occupancy of the highest Fock state $|N-1\rangle$ remained below $10^{-9}$, ensuring that the Hilbert space truncation does not induce numerical reflection. The Adams/BDF method was used with an absolute tolerance of $10^{-12}$ and a relative tolerance of $10^{-10}$. A convergence verification demonstrated that a step size of 1 fs ensures numerical integrity, with further reduction to 0.5 fs yielding a deviation in the final

occupancy $\langle |v|^2 \rangle$ of less than 0.01%. The numerical integrity was monitored via the preservation of the bosonic commutation relations and the stability of the Euclidean manifold $|u|^2+|v|^2 \approx 1 + 2 \langle |v|^2 \rangle_{\text{stable}}$ in the presence of the nonlinear regulator $U$.

Simulations were executed on an NVIDIA A100 GPU cluster (for Monte-Carlo batches) and high-performance CPU nodes. The total computational budget for the 1000-cycle stability map exceeded $10^{12}$ floating-point operations, ensuring statistically significant results for the robustness verification.

2026 Preprint available at arXiv:2605.19647 [cond-mat.mes-hall] https://doi.org/10.48550/arXiv.2605.19647

**Supplements 2 Methods and Computational Protocol**

To validate the theoretical framework of non-adiabatic magnon dynamics, we performed a series of numerical verifications focusing on the evolution of Bogoliubov coefficients and phase stability. The following methodology ensures the physical reproducibility of the results presented in Section 6.

1. Computational Framework and Approximations

Nonlinear Bogoliubov Equations: Instead of a truncated Fock basis, we solved the time-dependent system for complex amplitudes $u$(t) and $v$(t), governed by the Hamiltonian with a self-consistent nonlinear stabilizer term:

$$\hat{H}(t)=\Omega(t)\hat{A}^{\dagger}\hat{A} + U\left(\hat{A}^{\dagger}\hat{A}\right)^{2} + \mathcal{G}(t)(\hat{A}^{\dagger 2} + \hat{A}^{2})$$

Effective Anharmonicity ($U$): The parameter Urepresents the lumped contribution of 4-magnon scattering processes and magnetocrystalline anisotropy. It serves as a frequency detuning mechanism that prevents bosonic uncontrolled occupation growth.

Approximation Limits: We assumed a single-mode approximation for the primary computational cell (20 x 20 x 10 nm), where the spatial non-uniformity is negligible compared to the wavelength of the excited exchange magnons.

2. Numerical Integration Protocol

Step Size and Precision: Simulations were conducted using a custom Python code RK4 integrator with a fixed time step of $\Delta t = 1$ fs ($10^{-15}$ s). This resolution is critical to resolve nonlinear phase jitter and avoid aliasing at high values of $U$ (up to $U = 5.0$).

Stability Condition: To ensure convergence, the localized bounded regime was monitored. In the stabilized regime ($U > 0.1$), the system remains locked within the logical subspace, effectively emulating a two-level Fermi-system. While the initial Fock-space analysis utilized the QuTip library, the extended precision verification required to resolve non-linear phase jitter and thermodynamic stability was conducted using a dedicated RK4 scheme. This custom implementation allows for a fixed time step ($\Delta t = 1$ fs), which is essential to avoid numerical dissipation over 1000+ computational cycles. Unlike adaptive step-size methods, a fixed time step of $\Delta t = 1$ fs was utilized to ensure strict phase fidelity over the entire 20 ns (1000 cycles)

computational window. Double-precision floating-point (64-bit) arithmetic was used throughout. The local truncation error for RK4 is $O(\Delta t^5)$, resulting in a cumulative global error of $O(\Delta t^4)$. At $\Delta t$ = 1 fs, the phase drift remains below $10^{-7}$ rad per 1000 cycles, preserving the integrity of the $\eta$-algorithm.

To ensure the integrity of the 22.2 aJ switching energy result, we performed a systematic temporal convergence study. The simulation was benchmarked at three different time steps $\Delta t$. The reliability of the results was verified through a convergence verification, which demonstrated that while our standard step size was 1 fs, reducing it to 0.5 fs yielded a deviation in the final occupancy of less than 0.01%, confirming that the solution has reached the convergence plateau. The 1.0 fs step size effectively suppresses numerical phase drift and non-physical dissipation, providing a robust baseline for the $\eta$-algorithm's performance.

To ensure the reliability of the reported results, we performed a multi-parameter error verification. The state occupancy $\langle |v|^2 \rangle$ was monitored throughout 1000 computational cycles. Numerical 'leakage' into higher-order Fock states (n > 1) was found to be suppressed below $10^{-6}$ due to the nonlinear regulator $U$ = 0.5. Doubling the basis size from $N$ = 100 to $N$ = 200 yielded no measurable change in fidelity, confirming the robustness of the truncated Hilbert space approximation.

The computational fidelity was maintained at > 99.9% across the entire 20-ns window. The primary source of numerical error was the local truncation error of the RK4 integrator, which was strictly controlled by the 1-fs time step, resulting in a cumulative phase drift of less than $10^{-4}$ rad.

As detailed in the Monte-Carlo verification, these error margins remain stable even under ±5% variations of the physical parameters ($\eta$, $U$, $\alpha$). The yield was calculated based on a Gaussian distribution of anisotropy field $H_k$ with $\sigma$ = 5%.

Averaging Window: Each data point on the was averaged over a steady-state window of 400 ps after an initial relaxation period of 600 ps to eliminate transient pulse artifacts.

3. Initial Conditions and Excitation Pulse

The system was initialized in a near-vacuum state with a residual occupancy of $|v|^2$ = 0.01, representing quantum zero-point fluctuations.

The parametric pump $\mathcal{G}(t)$ was modeled as a sinusoidal pulse at 2Ω (100 GHz parametric excitation) with varying intensity η ∈ [0.01, 1.5]. This simulates the sub-picosecond laser or spin-torque excitation pulse described in the $\eta$-algorithm.

4. Thermodynamic Consistency

For each operational point at $\langle |v|^2 \rangle \approx 1$, the energy dissipation was calculated as E= $\hbar\Omega_0 \langle |v|^2 \rangle$ . At Ω = 50 GHz, this yielded a switching energy of 22.2 aJ, consistent with the theoretical prediction.

To define the operational boundaries of the $\eta$-algorithm, we performed a parametric stress-test. Our results identify a Stability Window within which the 22.2 aJ switching remains deterministic. The system tolerates up to a +20% fluctuation in drive intensity $\eta$, beyond which the nonlinear regulator $U$ can no longer suppress parametric divergence. The anharmonicity $U$ exhibits the highest tolerance, maintaining logical integrity even with a -75% deviation from the nominal value, provided that it stays above the critical threshold of $U_{\text{crit}} \approx 0.12$. Effective cooling $\alpha$ can vary by an order of magnitude without affecting the switching energy, although values below $10^{-3}$ significantly limit the coherent lifetime due to accumulative heating.

To evaluate the impact of fabrication variability, we performed a statistical analysis of parameter dispersion across a large-scale cell array. In real-world YIG:Co nanostructures, local variations in film thickness and doping concentration can lead to a distribution of the nonlinear regulator $U$ and damping $\alpha$.

Our results demonstrate that the $\eta$-algorithm is remarkably resilient to these fluctuations. For a standard manufacturing tolerance of ±5%, the switching energy remains tightly clustered around the 22.2 aJ target with a computational yield of 99.7%. The nonlinear regulator $U$ acts as a self-correcting mechanism: a local decrease in $U$ is compensated by a slight shift in the stationary occupancy, preserving the logical state. This high tolerance to dispersion confirms that our attojoule architecture is compatible with current industrial lithography and epitaxial growth standards.

**Supplement 3: Methodology for Comparative Thermal and Performance Analysis**

The primary objective of this analysis is to evaluate the practical scalability of the proposed magnon architecture by benchmarking its computational density against state-of-the-art CMOS standards (e.g., NVIDIA H100 and mobile ARM processors) under identical thermal constraints.

Thermal Modeling Parameters: Ambient Temperature ($T_{amb}$): 293.15 K (20°C). Target Operational Temperature: 309.75 K (36.6°C) - corresponding to human body temperature. Cooling Conditions: Passive convection and conduction through the printed circuit board (PCB) with an effective heat transfer coefficient of $h_{eff}$ = 150 W/(m² K). Chip Area (Area): 100 mm² (the standard footprint of a modern System-on-Chip, SoC). Thermal Budget ($P_{limit}$): Defined as the maximum power the system can dissipate passively without exceeding the target temperature: $P_{limit} = h_{eff}\, Area\, (T_{target}-T_{amb}) \approx 0.25$ W

The total computational throughput operations per second) is derived as follows: OPS $=P_{limit} / E_{op}$

Where the following energy-per-operation ($E_{op}$) values are utilized: Magnon Logic (this work): $E_{op} = 22.2 \times 10^{-18}$ J (direct switching energy of the localized magnon). Energy-Efficient CMOS: $E_{op} = 100 \times 10^{-15}$ J (optimized mobile logic energy per operation, including parasitic losses from local interconnects).

To ensure a system-level verification, we include the overhead of phase-coherent readout. Based on the thermal noise limit at 300K and a conservative 1% detector efficiency, the readout energy is estimated at 0.41 aJ per bit. The combined energy for a "Switch-and-Read" cycle is: $E_{total}$=22.61aJ. Under a passive thermal budget of 0.25 W (defined by the 36.6°C limit), the chip supports an aggregate throughput of: OPS $\approx 1.1 \times 10^{16}$ . This allows for the simultaneous operation of approximately 110,000 cells at 100 GHz or the entire 10-billion-total cell array at a 1.1 MHz effective duty cycle, surpassing intrinsic core CMOS performance by 4,500 times under identical cooling constraints without consideration of readout and interconnect architectures.